Bioactive Materials 33 (2024) 444–459

Contents lists available at ScienceDirect

Bioactive Materials

journal homepage: www.keaipublishing.com/en/journals/bioactive-materials

Engineered mesenchymal stem cell-derived small extracellular vesicles for diabetic retinopathy therapy through HIF-1α/EZH2/PGC-1α pathway

Fengtian Sun [a,b,1], Yuntong Sun [a,b,1], Xiaoling Wang [a,c,1], Junyan Zhu [a], Shenyuan Chen [a], Yifan Yu [a], Mengyao Zhu [a], Wenrong Xu [a,**], Hui Qian [a,d,*]

[a] Jiangsu Key Laboratory of Medical Science and Laboratory Medicine, Department of Laboratory Medicine, School of Medicine, Jiangsu University, Zhenjiang, 212013, Jiangsu, China
[b] Department of Clinical Laboratory, Affiliated Jinhua Hospital, Zhejiang University School of Medicine, Jinhua, 321000, Zhejiang, China
[c] Department of Laboratory Medicine, Zhongshan Hospital (Xiamen), Fudan University, Xiamen, 361006, Fujian, China
[d] NHC Key Laboratory of Medical Embryogenesis and Developmental Molecular Biology & Shanghai Key Laboratory of Embryo and Reproduction Engineering, Shanghai, 200040, China

ARTICLE INFO

Keywords:
Small extracellular vesicles
Diabetic retinopathy
Mesenchymal stem cell
MiRNA
Engineering

ABSTRACT

Diabetic retinopathy (DR) is a leading cause of blindness worldwide with limited treatment options. Mesenchymal stem cell-derived small extracellular vesicles (MSC-sEVs) hold promise as a cell-free therapy for retinal diseases. In this study, we present evidence that the intravitreal injection of MSC-sEVs improved retinal function and alleviated retinal apoptosis, inflammation, and angiogenesis in both db/db mice and streptozotocin-induced diabetic rats. Mechanistically, hyperglycemia-induced activation of hypoxia-inducible factor-1α (HIF-1α) inhibited the tripartite motif 21 (TRIM21)-mediated ubiquitination and degradation of enhancer of zeste homologue 2 (EZH2), ultimately resulting in the downregulation of peroxisome proliferator-activated receptor-γ coactivator-1α (PGC-1α) through EZH2-induced methylation modification. The presence of miR-5068 and miR-10228 in MSC-sEVs targeted the HIF-1α/EZH2/PGC-1α pathway. The blockade of miR-5068 and miR-10228 abolished the retinal therapeutic effects of MSC-sEVs. Additionally, we engineered MSC-sEVs with elevated levels of miR-5068 and miR-10228 to enhance retinal repair efficiency. Together, our findings provide novel insights into the mechanism underlying DR progress and highlight the potential of MSC-sEVs, especially engineered MSC-sEVs, as a therapeutic option for DR.

1. Introduction

Diabetic retinopathy (DR) is a significant microvascular complication of diabetes and a leading cause of blindness in working-age adults [1,2]. The pathogenesis of DR is mainly characterized by the release of inflammatory and oxidative cytokines, resulting in retinal cell loss, vessel dysfunction, and neovascularization [3–5]. Hyperglycaemia-induced pathological angiogenesis of retinal endothelial cells plays a central role in DR progress [6,7]. Current treatments involve surgical neovascular ablation and antiangiogenic drug injection, but their effectiveness is limited, and they carry the risk of disease recurrence and severe adverse reactions [8,9]. Therefore, identifying progressive mechanisms and developing effective treatments for DR are crucial.

Mesenchymal stem cell (MSC) transplantation has demonstrated regenerative benefits in various diseases [10,11]. Although MSC transplantation exhibits repairing effects in retinal injury, its application is limited due to many factors such as malignant transformation, tumor-associated fibroblasts metastasis, and low risk of implantation in vivo [12]. Recent research indicates the release of small extracellular

Peer review under responsibility of KeAi Communications Co., Ltd.
* Corresponding author.Jiangsu Key Laboratory of Medical Science and Laboratory Medicine, School of Medicine, Jiangsu University, 301# Xuefu Road, Zhenjiang, 212013, Jiangsu, China.
** Corresponding author. Jiangsu Key Laboratory of Medical Science and Laboratory Medicine, School of Medicine, Jiangsu University, 301# Xuefu Road, Zhenjiang, 212013, Jiangsu, China.
E-mail addresses: icls@ujs.edu.cn (W. Xu), lstmmmlst@163.com (H. Qian).
[1] These authors contributed equally to this work.

https://doi.org/10.1016/j.bioactmat.2023.11.008
Received 6 June 2023; Received in revised form 17 October 2023; Accepted 15 November 2023

vesicles (sEVs) as a major mechanism underlying MSC-based cell therapy [13]. As a type of nano-sized membranous vesicles, sEVs mediate intercellular communications by transporting various bioactive molecules such as nucleic acids, proteins, and lipids [14]. MSC-derived sEVs (MSC-sEVs) therapy is considered a novel cell-free strategy for treating various disorders [15]. The therapeutic potential of MSC-sEVs has attracted significant interest in the field of ocular diseases [16]. The administration of MSC-sEVs has been found to have an inhibitory effect on neuro-inflammation and apoptosis in a rat model of retinal ischemia [17]. Our previous study has also demonstrated the ability of MSC-sEVs to reduce apoptosis and oxidative stress in streptozotocin (STZ)-induced diabetic rats [18]. However, the exact function and mechanism of MSC-sEVs in hyperglycemia-induced retinal vascular injury remain unclear. Due to their stability and biocompatibility, sEVs serve as safe and efficient delivery tools [19]. The plasma membrane structure of sEVs enables them to protect cargos from degradation, which promotes the engineering concept of sEVs to enhance their repairing effects [20]. Currently, the loading of therapeutic molecules or drugs into sEVs has emerged as an effective modification strategy [21]. The development of engineered MSC-sEVs may offer new avenues for more efficient cell-free therapy for DR.

Increasing studies have indicated that sEVs contain enriched microRNAs (miRNAs), which are noncoding RNAs with the length of about 22 nucleotides and negatively regulate the expression of target genes [22]. MiRNA delivery has been widely reported to mediate the therapeutic value of MSC-sEVs in various diseases [23]. Importantly, emerging evidence suggests that DICER and Argonaute2 (AGO2) knockdown impairs the effects of MSC-sEVs on preventing retinal neuronal precursor cells from viability loss [24]. These genes are involved in sorting miRNAs into sEVs, indicating that MSC-sEVs-mediated retinal protection may depend on miRNA-related mechanisms. It has also been observed that dysregulated miRNA expression is closely linked to retinal injury caused by hyperglycemia [25]. Furthermore, identifying the key miRNAs in MSC-sEVs could be crucial for developing engineered MSC-sEVs for the treatment of DR.

In this study, we established two diabetes models including db/db mice and STZ-induced diabetic rats to evaluate the therapeutic potential of MSC-sEVs in hyperglycemia-induced retinal injury. Moreover, we investigated the underlying molecular mechanism using miRNA sequencing, transcriptome sequencing, mass spectrometry analysis and bisulfite sequencing polymerase chain reaction (BSP). Furthermore, we developed engineered MSC-sEVs with increased levels of therapeutic molecules and evaluated their efficiency in retinal repair in vivo.

2. Materials and methods

2.1. Ethics statement

The study was approved by the Ethics Committee for Experimental Animals of Jiangsu University (UJS-IACUC-2021110301).

2.2. Cell culture and identification

MSCs were isolated from fresh umbilical cords with the consent of mothers at the Affiliated Hospital of Jiangsu University. The umbilical cords were dissected into 1-mm^2-sized fragments after removing cord blood. These fragments were then cultured in minimal essential medium alpha (α-MEM; Invitrogen, Grand Island, NY, USA) supplemented with 15 % fetal bovine serum (FBS; Gibco, Grand Island, USA) at 37 °C with 5 % CO_2. The medium was refreshed every 3 days to ensure optimal conditions for cell growth. Primary cells were harvested using trypsin and passaged for further expansion. The MSCs were then cultured in α-MEM (Invitrogen, Grand Island, NY, USA) supplemented with 10 % FBS (Gibco, Grand Island, USA) at 37 °C with 5 % CO_2. MSCs at passage 3 were cultured in osteogenic medium (Cyagen Biosciences, CA, USA) or adipogenic medium (Cyagen Biosciences, CA, USA) for 2 weeks. Following the differentiation induction, MSCs were stained with Alizarin Red S or Oil Red O to assess their osteogenic or adipogenic potential. Flow cytometry assay was used to detect the markers of MSCs including CD29, CD73, CD105, CD11b, CD34 and CD45.

Human fetal lung fibroblast 1 (HFL1), retinal microvascular endothelial cells (RMECs), and human embryonic kidney 293T (HEK293T) cells were purchased from the cell bank of the Chinese Academy of Sciences. These cell lines were cultured in low glucose (LG) Dulbecco's modified Eagle's medium (DMEM; Invitrogen, Grand Island, NY, USA) supplemented with 10 % FBS (Gibco, Grand Island, USA) at 37 °C with 5 % CO_2.

2.3. Isolation and characterization of sEVs

The culture supernatants of MSC or HFL1 cultured in sEVs-depleted medium (complete medium after overnight centrifugation at 100,000g) were collected after 48 h. The collected supernatants were filtered through a 0.22-μm filter and centrifuged at 300g for 5 min, 2,000g for 10 min, and 10,000g for 30 min to remove cells, cell debris and organelles. MSC-sEVs and HFL1-derived sEVs (HFL1-sEVs) were precipitated by ultracentrifugation at 100,000g for 3 h, resuspended in PBS, passed through a 0.22-μm filter, and stored at −80 °C.

The morphology of sEVs was observed using transmission electron microscopy (TEM; FEI Tecnai 12, Philips, Netherlands). The size distribution and particle count of sEVs were determined using nanoparticle tracking analysis (NTA; NanoSight, Amesbury, UK). The protein markers of sEVs including tumor susceptibility gene 101 (TSG101), Alix, CD9, CD63, and calnexin were detected by Western blot.

2.4. Animal model and treatment

The homozygous db/db mice and db/m heterozygotes from the same colony were purchased from Cavens Laboratory Animal Co. Ltd. (Changzhou, China). Sprague-Dawley rats, 8 weeks old and weighing 200 ± 20 g, were purchased from the Animal Centre of Jiangsu University. The rats were randomly divided into diabetic and normal groups. Diabetic group was fed with 45 % high-fat diets for 4 weeks, followed by the intravenous injection of STZ (35 mg/kg in 0.1 M citrate-buffered saline, pH 4.5; Sigma-Aldrich, St. Louis, USA) via the tail vein. Three days later, the rats with fasting blood glucose level above 16.7 mM were classified as diabetic rats. The normal group was fed with normal diets and injected with citrate-buffered saline (0.1 M, pH 4.5) through the tail vein. All animals were housed in a pathogen-free environment with a 12 h light/dark cycle at a temperature of 25 °C. They had unrestricted access to food and water. For intravitreal injection, the collected sEVs (MSC-sEVs, HFL1-sEVs, miRNA inhibitors-loaded MSC-sEVs or miRNA mimics-loaded MSC-sEVs) were adjusted to a concentration of 1×10^7 particles/μL and injected at 1 μL into each vitreous chamber of 12-week-old db/db mice or diabetic rats at 12 weeks after STZ injection with a 33-G Hamilton syringe (Hamilton Company, USA). Db/m and db/db mice at 28 weeks of age or normal rats and diabetic rats at 28 weeks after STZ injection were euthanized using 4 % isoflurane. The eyeballs were then collected for further analysis. Db/db mice and STZ-induced diabetic rats were randomly divided into different groups at the designated time point of intravitreal injection. A total of five db/db mice and seven STZ-induced diabetic rats died before the intravitreal injection with MSC-sEVs, inhibitors-loaded MSC-sEVs and engineered MSC-sEVs. No animals died after the intravitreal injection. The starting number of animals in each group was 16 after grouping. After sEVs injection, researchers who were not aware of the group information randomly selected animals from each group for the corresponding experiment, evaluated the outcome, and analyzed the data. The number of animals in each experiment is shown in Figure legend. After the experiment, the remaining animals were euthanized using 4 % isoflurane. During the study period, no experimental results were discarded.

2.5. Electroretinography (ERG) analysis

After overnight dark adaptation, the animals were anesthetized with an intraperitoneal injection of sodium pentobarbital and positioned on a stage. Under dim red light conditions, the corneas of animals were anesthetized with 0.5 % proxymetacaine. The ground electrodes, reference electrodes and corneal contact electrodes were then placed on the animal. White flashes with the intensity of 3.0 cd s/m^2 were adopted to induce the responses. The UTAS Visual Diagnostic System (LKC Technologies, USA) was used to record the scotopic a/b-wave.

2.6. Optokinetic response (OKR)

To assess the OKR, a computer-based visual acuity response test (OptoMotry, Cerebral Mechanics) was used. The experiment involved placing animals on a central platform surrounded by four computer monitors that displayed alternating black and white vertical bars. The animals were monitored by a camera placed above. The head movement behavior of animals was recorded by two investigators who were unaware of the experimental group information. The test began by projecting a low spatial frequency grating (0.042 cycles/degree) that rotated at a speed of 12°/s with 100 % contrast. Visual acuity was defined as the highest grating frequency at which optomotor response could be reliably detected.

2.7. Retinal hematoxylin and eosin (H&E) staining and immunohistochemistry

After the enucleation procedure, the retinal tissues were rapidly isolated, fixed in 4 % paraformaldehyde overnight and embedded in paraffin. Then, 4-μm sections were prepared and stained with H&E for the observation of retinal morphology. For immunohistochemistry analysis, the deparaffinized retinal tissue sections were treated with 3 % hydrogen peroxide to inhibit the activity of endogenous peroxidase and soaked in boiled citrate buffer (pH 6.0, 10 mM) to repair antigens. Tissue sections were then blocked with 5 % bovine serum albumin (BSA) and incubated with primary antibody against vascular endothelial growth factor (VEGF; 1:100, Proteintech, 19003-1-AP, China) or cleaved caspase-3 (1:100, CST, 9661, USA) overnight. Subsequently, the sections were incubated with secondary antibody for 1 h, visualized using diaminobenzidine (Boster, Wuhan, China), counterstained with hematoxylin and photographed under a microscope (DP73, Olympus, Tokyo, Japan).

2.8. Terminal deoxynucleotidyl transferase-mediated deoxyuridine triphosphate nick end labeling (TUNEL) staining

TUNEL staining was performed according to the manufacturer's instructions (Vazyme, Nanjing, China). After deparaffinization, each section was incubated with 100 μL of proteinase K solution at room temperature for 20 min, balanced in 100 μL of 1 × equilibration buffer for 30 min, and treated with 100 μL of TDT buffer for 1 h at 37 °C to label apoptotic cells. The nuclei were counterstained with Hoechst 33,342 (Sigma-Aldrich, St. Louis, USA). Finally, the sections were visualized using a confocal microscope (DeltaVision Elite, GE, USA).

2.9. Retinal trypsin digestion assay

Eyeballs were fixed in 4 % paraformaldehyde for 12 h. The retinas were carefully separated, subjected to digestion at 37 °C for 2 h, stained with periodic acid-Schiff (Sbjbio, Nanjing, China), and counterstained with hematoxylin. Acellular vessels were observed and quantified by examining 10 random fields under a microscope (DP73, Olympus, Tokyo, Japan).

2.10. Evans blue dye leak assay

Evans blue dye leak assay was used to detect the retinal vascular permeability. The animals were anesthetized with intraperitoneal ketamine (80 mg/kg) and xylazine (4 mg/kg) and injected with Evans blue (45 mg/kg; Sbjbio, Nanjing, China) through the jugular vein. After circulation for 2 h, the animals were perfused with saline and 4 % paraformaldehyde through the left ventricle. The retinas were carefully separated and dried for 6 h to measure their dry weight. The residual Evans blue dye in the retina was isolated using 200 μL of formamide (Sigma-Aldrich, St. Louis, USA) at 78 °C overnight, followed by centrifugation at 12,000g for 30 min. The absorbance of the supernatant was detected at 620 nm and 740 nm using a spectrophotometer (FLX800, BioTek, USA), and the concentration of Evans blue was quantified based on a standard curve. Finally, the Evans blue content was normalized by retinal dry weight for subsequent analysis.

2.11. Transcriptome sequencing

Total RNAs were isolated from retinal tissues of the mice in db/db and db/db + MSC-sEVs groups. Cutadapt, Hisat2 and Cuffdiff software packages were used to compare high-quality reads to the genome, obtain the FPKM value, and calculate the differentially expressed genes. In addition, ClusterProfiler R package was used for KEGG enrichment analysis of different cluster genes.

2.12. MiRNA sequencing

The miRNA sequencing of MSC-sEVs and HFL1-sEVs was performed by OE Biotech (Shanghai, China). MSC-sEVs and HFL1-sEVs were purified from 200 mL of cell supernatants respectively, followed by the extraction of total RNAs. A total of 5 μg RNAs were ligated to adaptors at each end, reverse transcribed to cDNA, and sequenced using the Illumina HiSeq sequencer. Differentially expressed miRNAs were analyzed with a significance threshold of P value < 0.05.

2.13. LC-MS/MS

RMECs transfected with hypoxia-inducible factor-1α (HIF-1α) siRNA or NC were subjected to digestion with the sequencing-grade trypsin. The samples were analyzed using LC-MS/MS to determine the differential expressed proteins. Moreover, RMECs were lysed in Co-IP buffer, and the lysates were immunoprecipitated using an enhancer of zeste homologue 2 (EZH2) antibody (1:100, CST, 5246, USA). Subsequently, the co-immunoprecipitation (Co-IP) samples were analyzed using LC-MS/MS to identify the proteins bound to EZH2.

2.14. BSP analysis

The Genomic DNA Extraction Kit (TIANGEN, DP304, Beijing, China) was used to isolate genomic DNA from all samples. The isolated DNA was subjected to bisulfite treatment. Subsequently, 1 μL of the bisulfite modified DNA from each sample was mixed with primers, dNTP, Taq buffer, Taq enzyme and ddH_2O for PCR analysis. The reaction mixture was initially predenatured at 95 °C for 5 min and amplified using a PCR program (35 cycles of 94 °C for 30 s, 55 °C for 30 s, and 72 °C for 40 s, and a final extension at 72 °C for 5 min). The PCR products obtained were then cloned into the pTG19-T vector and utilized for sequencing analysis.

2.15. Western blot

Total protein from sEVs, cells and retinal tissues was isolated using radioimmunoprecipitation assay lysis buffer. Protein samples with equal amounts were separated through sodium dodecyl sulfate polyacrylamide gel electrophoresis and transferred onto polyvinylidene

difluoride membranes (Millipore, USA). After blocking with 5 % skim milk for 1 h, the membranes were incubated with primary antibodies overnight at 4 °C, followed by the incubation with horseradish peroxidase-conjugated secondary antibodies (SAB, USA) at 37 °C for 1 h. Finally, the protein bands were detected using an enhanced chemiluminescence. The primary antibodies used in this study are listed in Supplementary Table S1.

2.16. RNA extraction and qRT-PCR

Total RNA from retinal tissues and cells was isolated using Trizol reagent (Gibco, Grand Island, USA), and RNA from sEVs was extracted using MiRNeasy micro kit (Qiagen, Germany). The gene level was determined using reverse transcription (Vazyme, Nanjing, China) and qRT-PCR (Vazyme, Nanjing, China). MiRNA was converted to cDNA using a MicroRNA Reverse Transcription Kit (Qiagen, Germany). For the detection of miR-5068 and miR-10228 in sEVs, the synthetic miRNA *Caenorhabditis elegans* miR-39 (cel-miR-39; 5 fmol/μL), Sequence: 5'-UCACCGGGUGUAAAUCAGCUUG-3′, was used as an exogenous control as previously reported [26]. The primer sequences are listed in Supplementary Table S2.

2.17. Cell treatment and transfection in vitro

In vitro, RMECs were exposed to high glucose (HG) medium (30 mM) for 48 h to mimic diabetic injury. After washing with PBS, the RMECs were then incubated with fresh HG medium supplemented with sEVs (1×10^7 particles/mL) for 24 h.

The RMECs and HEK293T cells, with a confluency of approximately 70 %, were transfected with siRNA, siRNA NC, miRNA mimics, miRNA mimics NC, miRNA inhibitors, or miRNA inhibitors NC using Lipofectamine 2000 (Life Technologies, Carlsbad, CA, USA) in serum-free medium. After 6 h, the cells were cultured in complete medium supplemented with 10 % FBS (Gibco, Grand Island, USA). The sequences of siRNA, siRNA NC, miRNA mimics, miRNA mimics NC, miRNA inhibitors, and miRNA inhibitors NC are listed in Supplementary Table S3.

2.18. Immunofluorescence staining

After deparaffinization, retinal sections were treated with boiled citrate buffer (pH 6.0, 10 mM) to repair antigens, blocked with 5 % BSA for 1 h and incubated with the primary antibody at 4 °C overnight. For the immunofluorescence staining of cells, RMECs were fixed on the slides with 4 % paraformaldehyde for 30 min, permeabilized with 0.1 % Triton X-100 for 15 min, blocked with 5 % BSA for 1 h and incubated with the primary antibody overnight at 4 °C. Next, the fluorescent-labeled secondary antibody (Sigma-Aldrich, St. Louis, USA) was applied to the sections for 1 h at 37 °C. The nuclei of retinal tissues or cells were then stained with Hoechst 33,342 (Sigma-Aldrich, St. Louis, USA). The sections were observed using a confocal microscope (DeltaVision Elite, GE, USA). The primary antibodies included HIF-1α (1:100, CST, 36,169, USA) and EZH2 (1:100, Proteintech, 66476-1-Ig, China).

2.19. Co-IP assay

Cells were lysed in Co-IP buffer and incubated with the HIF-1α antibody (1:100, CST, 36,169, USA) or EZH2 antibody (1:100, CST, 5246, USA) overnight at 4 °C. The lysates were then treated with protein A agarose (Beyotime, China) for 4 h. After incubation, the protein complexes were washed with Co-IP buffer and detected using Western blot.

2.20. Chromatin immunoprecipitation (ChIP) assay

The treated RMECs were incubated with formaldehyde for 10 min to induce cross-linking. Subsequently, ultrasonication was performed to generate DNA fragments. The EZH2 antibody (1:100, CST, 5246, USA), histone H3 lysine 27 trimethylation (H3K27me3) antibody (1:100, CST, 9733, USA), IgG, and magnetic beads were added to the samples. Immunoprecipitated DNA was analyzed using qRT-PCR. The following primers were used to detect the promoter sequence of peroxisome proliferator-activated receptor-γ coactivator-1α (PGC-1α).

Forward: 5′-TTACTTCACTGAGGCAGAGGGCT-3′
Reverse: 5′-AAGTAGGCTGGGCTGTCACTCA-3′.

2.21. CCK8 assay

The treated RMECs were resuspended and seeded into 96-well plates at a density of 3000 cells per well. After incubation for 24, 48, 72 and 96 h, the previous medium was discarded, and 100 μL of fresh medium containing 10 μL of CCK8 (Vazyme, Nanjing, China) was added to each well. The cells were then incubated for an additional 3 h. The absorbance in each well was measured at 450 nm using a spectrophotometer (FLX800, BioTek, USA).

2.22. EdU staining

The treated RMECs were fixed in 4 % paraformaldehyde for 30 min and permeabilized with 0.1 % Triton X-100 for 15 min at room temperature. After washing with PBS, the RMECs were stained using the BeyoClick™ EdU-488 kit (Beyotime, Shanghai, China) and observed under a microscope (DP73, Olympus, Tokyo, Japan).

2.23. Transwell migration assay

The treated RMECs were resuspended in serum-free medium and seeded into the upper chamber at a density of 3×10^4 cells per chamber. Subsequently, 500 μL of fresh medium supplemented with 10 % FBS was added to the lower chamber. After incubation for 24 h, the migrated cells were fixed with 4 % paraformaldehyde, stained with crystal violet, and photographed under a microscope (DP73, Olympus, Tokyo, Japan).

2.24. Tube formation assay

Each well of 24-well plates was coated with 200 μL of Matrigel (BD Biosciences, USA). The treated RMECs were seeded on Matrigel (3×10^4 cells/well) and then incubated for 12 h. The cells were photographed under a microscope (DP73, Olympus, Tokyo, Japan).

2.25. Electroporation

A total of 45 μL of MSC-sEVs (1×10^6 particles/μL) were mixed with 5 μL of miRNA mimics or inhibitors (1 μg/μL) in a reaction cup, followed by electroporation using a CUY21EDIT II electroporator (BEX, Japan) at 110 V and 940 μF. After electroporation, the MSC-sEVs were washed with PBS and subjected to ultracentrifugation at 100,000g for 3 h to remove unbound nucleic acids. To assess the loading efficiency, the miRNA mimics and inhibitors were labeled with FITC. The FITC fluorescence of the mixture containing FITC-labeled miRNA mimics or inhibitors and MSC-sEVs was measured using a fluorescence detection plate reader. After electroporation, the miRNA mimics or inhibitors-loaded MSC-sEVs were precipitated by ultracentrifugation, and the unloaded FITC-miRNA mimics or inhibitors were collected from the supernatant. The FITC fluorescence of the supernatant (unloaded miRNA mimics or inhibitors) was measured using a fluorescence detection plate reader and quantified using a calibration curve. The loading efficiency was calculated using the equation below:

$$\text{Loading efficiency} = \frac{\text{Input miRNA} - \text{free miRNA}}{\text{Input miRNA}}$$

2.26. Statistical analysis

All statistical analysis was performed using GraphPad Prism software (GraphPad, San Diego, USA). All data are presented as the means ± SEM. Unpaired Student's t-test was used to assess and compare the differences between two distinct groups. Analysis of variance with Newman-Keuls test or Bonferroni test was utilized to evaluate and compare the differences among multiple groups. P value < 0.05 was considered statistically significant.

3. Results

3.1. Characterization of MSCs and sEVs

MSCs which were isolated from human umbilical cords displayed fibroblast-like growth (Supplementary Figs. S1a and b). After adipogenic and osteogenic medium inductions, positive staining results of Oil Red O and Alizarin Red S were obtained (Supplementary Figs. S1c and d). The flow cytometry assay results revealed that MSCs expressed CD29, CD73, and CD105 and negatively expressed CD11b, CD34, and CD45 (Supplementary Fig. S1e). These findings confirm the successful isolation of MSCs with multidirectional differentiation potential. Subsequently, we purified sEVs from the conditioned medium of MSCs and HFL1. Since the cell morphologies of MSCs and HFL1 are similar, HFL1-sEVs were utilized as control to demonstrate the specificity of MSC-sEVs in DR therapy. The results of TEM, NTA and Western blot showed that both MSC-sEVs and HFL1-sEVs displayed the sphere-shaped morphology with an average diameter of around 160 nm, expressed specific proteins associated with sEVs such as TSG101, Alix, CD9, CD63 and β-actin, and showed negative expression of calnexin (Fig. 1a–c).

3.2. Retinal therapeutic effects of MSC-sEVs in db/db mice

To evaluate the retinal therapeutic efficacy of MSC-sEVs, db/db mice were used as the animal model, and MSC-sEVs were administered intravitreally. Immunofluorescence staining revealed a widespread distribution of MSC-sEVs in the various layers of retinal cells. Co-staining of PKH26 and Isolectin B4 (IB4) demonstrated that a portion of MSC-sEVs were absorbed by retinal vascular endothelial cells (Fig. 2a). ERG analysis revealed that MSC-sEVs protected retinal functions against diabetic microenvironment, quantified by the increased amplitudes of a-wave and b-wave, whereas HFL1-sEVs did not provide such protective effect (Fig. 2b). The functional visual improvement mediated by MSC-sEVs in db/db mice was further validated by OKR experiments (Supplementary Fig. S2). The H&E staining of retinal sections demonstrated that db/db mice exhibited retinal degeneration and decreased retinal thickness, while MSC-sEVs treatment resulted in the preservation of retinal integrity and improvement of retinal thickness (Fig. 2c). Additionally, TUNEL assay presented that MSC-sEVs effectively attenuated retinal cell apoptosis induced by diabetic conditions (Fig. 2d). Furthermore, the hyperglycemia-induced downregulation of proliferating cell nuclear antigen (PCNA) and bcl-2 and upregulation of bax in retinal tissues were ameliorated by MSC-sEVs (Fig. 2e). Dihydroethidium (DHE) staining and malondialdehyde (MDA) detection showed that MSC-sEVs treatment reduced oxidative stress levels in the retinas of db/db mice (Supplementary Figs. S3a–c). The db/db mice treated with MSC-sEVs exhibited decreased levels of inflammatory cytokines including interleukin-1β (IL-1β), interleukin-6 (IL-6), tumor necrosis factor-α (TNF-α), and transforming growth factor-β (TGF-β) in their retinas (Fig. 2f). Furthermore, intravitreal MSC-sEVs delivery inhibited the retinal expression of VEGF (Fig. 2g). Western blot and Evans blue leakage assay results revealed that MSC-sEVs effectively prevented hyperglycemia-induced reductions in tight junction protein expression such as claudin-5, occludin and zona occludens-1 (ZO-1) and reduced vascular permeability (Fig. 2h and i). Retinal trypsin digestion assay confirmed the increased formation of acellular capillaries in db/db mice and the restorative impact of MSC-sEVs treatment on the retinal vascular structure (Fig. 2j). These findings suggest that MSC-sEVs exert therapeutic roles in DR by improving retinal function and alleviating retinal apoptosis, inflammation, and angiogenesis.

3.3. MSC-sEVs ameliorate retinal injury by inhibiting HIF-1α expression

To explore the mechanism underlying the retinal protective effects of MSC-sEVs, we conducted transcriptome sequencing of retinal tissues following MSC-sEVs treatment. Gene ontology analysis for biological processes revealed significant changes in genes associated with the response to hypoxia (Supplementary Fig. S4). Additionally, Kyoto Encyclopedia of Genes and Genomes (KEGG) pathway analysis identified that numerous differentially expressed genes were enriched in the HIF-1α signaling pathway (Fig. 3a). It is reported that long-term hyperglycemia can cause retinal hypoxia during DR progress [27]. HIF-1α has been identified as a significant therapeutic target for DR [28]. Therefore, we focused on determining whether MSC-sEVs alleviate DR

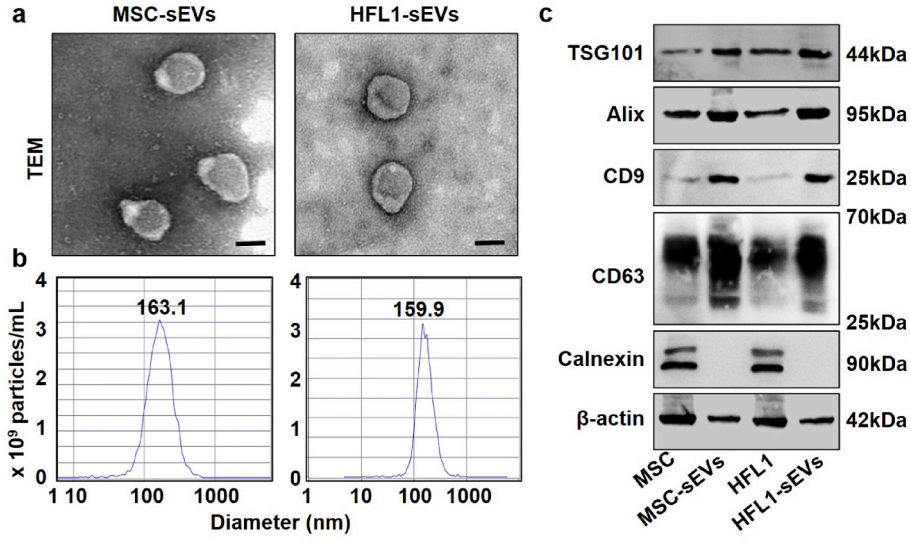

Fig. 1. Characterization of sEVs. (**a**) TEM images of MSC-sEVs and HFL1-sEVs. Scale bars, 100 nm. (**b**) NTA for the size distribution and particle number of MSC-sEVs and HFL1-sEVs. (**c**) Western blot for protein markers of MSC-sEVs and HFL1-sEVs.

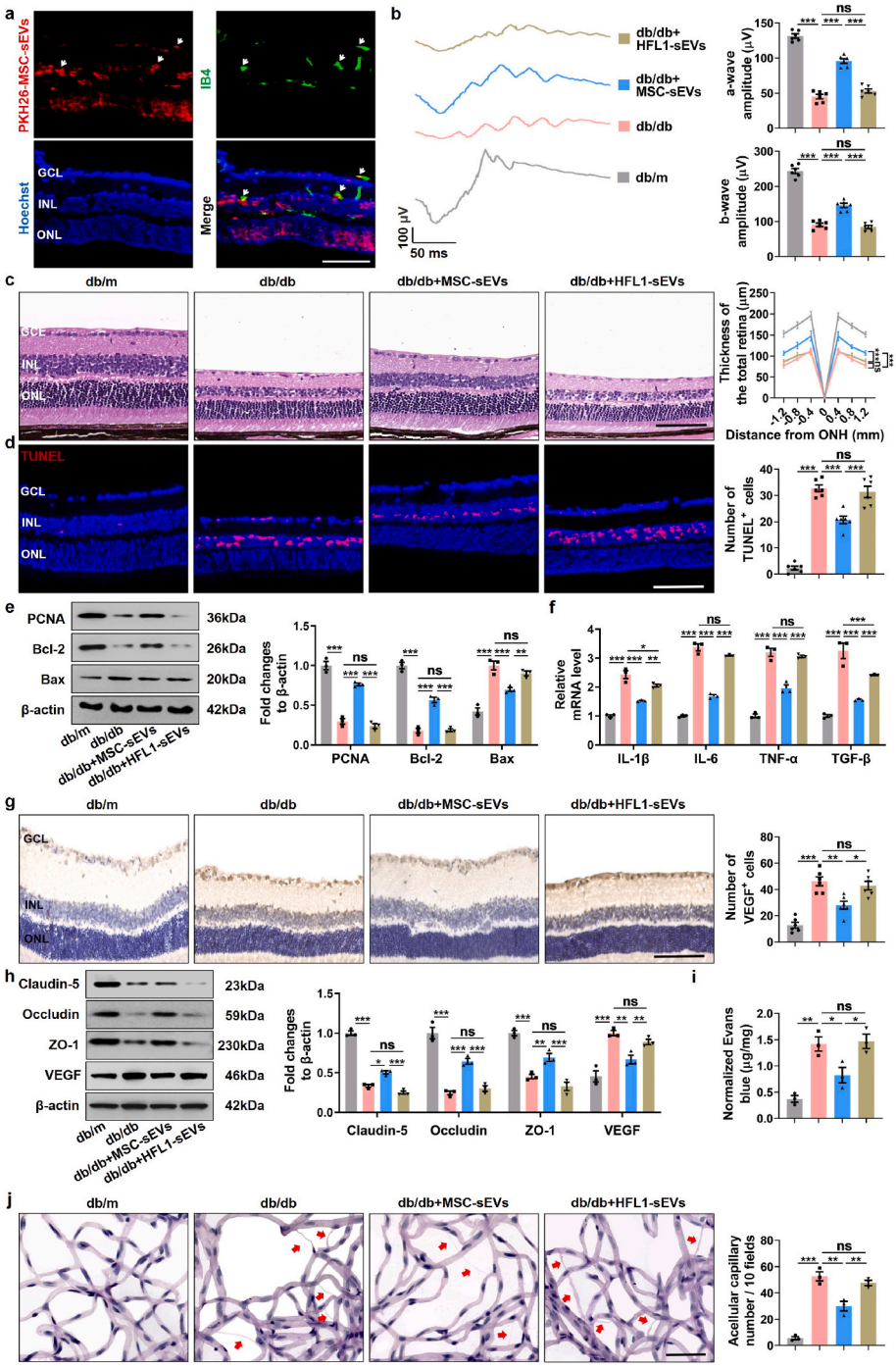

Fig. 2. Intravitreal injection of MSC-sEVs alleviates retinal injury in db/db mice. (**a**) Representative images of retinal sections of db/db mice treated with the PKH26-labeled MSC-sEVs. PKH26, red; IB4, green. Scale bars, 100 μm. (**b**) Representative ERG waveforms and the corresponding analysis of amplitudes of a-wave and b-wave (n = 6). (**c**) H&E staining of retinal tissues and the corresponding quantitative analysis of retinal thickness. Scale bars, 100 μm. (**d**) TUNEL staining of retinal tissues. Scale bars, 100 μm. (**e**) Western blot for the retinal expression of PCNA, Bcl-2 and Bax. (**f**) qRT-PCR for the relative mRNA levels of IL-1β, IL-6, TNF-α and TGF-β (n = 3). (**g**) Immunohistochemistry images of VEGF in retinal tissues. Scale bars, 100 μm. (**h**) Western blot for the retinal expression of claudin-5, occludin and ZO-1. (**i**) Quantitative analysis of the residual Evans blue dye in the retina (n = 3). (**j**) Retinal trypsin digestion assay. Scale bar, 50 μm. All data are presented as means ± SEM. ns, not significant, $^{*}P < 0.05$, $^{**}P < 0.01$ and $^{***}P < 0.001$. GCL, ganglion cell layer; INL, inner nuclear layer; ONL, outer nuclear layer.

by inhibiting HIF-1α expression. Immunofluorescence staining and Western blot results demonstrated that hyperglycemia conditions promoted the accumulation of HIF-1α in retinal tissues, whereas MSC-sEVs reduced the expression of HIF-1α (Fig. 3b and c). By measuring the expression of HIF-1α in RMECs, we confirmed that MSC-sEVs could restore the upregulation of HIF-1α triggered by HG medium and prevent HIF-1α nuclear transcription (Fig. 3d and e). To verify the significance of MSC-sEVs-mediated HIF-1α inhibition in retinal recovery, we treated RMECs with MSC-sEVs in the presence of dimethyloxallyl glycine (DMOG), which is an agonist of HIF-1α. Immunofluorescence staining showed that PKH26-labeled MSC-sEVs could be internalized by RMECs after co-incubation (Fig. 3f). We observed that HFL1-sEVs had limited effects to alleviate HG-induced cell dysfunction. In contrast, treatment with MSC-sEVs effectively mitigated the proliferation, migration, and

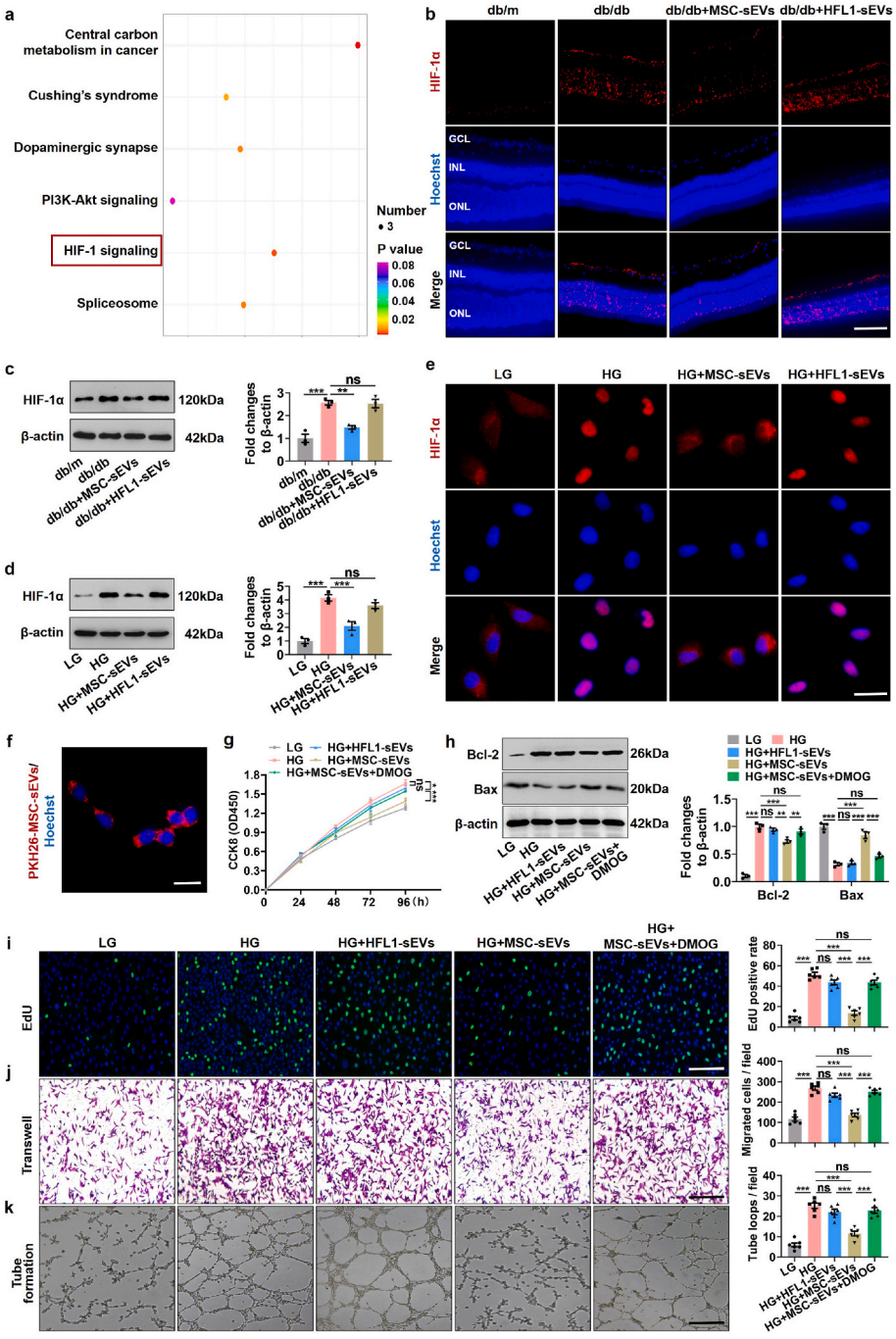

Fig. 3. MSC-sEVs-mediated the inhibition of HIF-1α. (**a**) Pathway analysis for the differentially expressed genes in db/db group and db/db + MSC-sEVs group by transcriptome sequencing of retinal tissues. (**b**) Immunofluorescence staining images of retinal tissues showing HIF-1α expression. Scale bars, 100 μm. (**c**) Western blot for the retinal expression of HIF-1α. (**d**) Western blot for the expression of HIF-1α in RMECs. (**e**) Immunofluorescence staining images of RMECs showing HIF-1α expression. Scale bars, 25 μm. (**f**) The internalization of PKH26-labeled MSC-sEVs by RMECs. Scale bars, 25 μm. (**g**) CCK8 assay for the proliferation of RMECs (n = 4). (**h**) Western blot for the expression of Bcl-2 and Bax in RMECs. (**i**) EdU staining of RMECs (n = 6). Scale bar, 100 μm. (**j**) Transwell assay for the migration of RMECs (n = 6). Scale bar, 100 μm. (**k**) Tube formation assay of RMECs (n = 6). Scale bar, 100 μm. All data are presented as means ± SEM. ns, not significant, $^{*}P < 0.05$, $^{**}P < 0.01$ and $^{***}P < 0.001$. GCL, ganglion cell layer; INL, inner nuclear layer; ONL, outer nuclear layer.

tube formation of RMECs under HG conditions. Notably, when RMECs were exposed to both MSC-sEVs and DMOG treatment, the beneficial effects of MSC-sEVs were significantly impaired (Fig. 3g–k). These results indicate that MSC-sEVs-mediated retinal therapy relies on the inhibition of HIF-1α.

3.4. *HIF-1α inhibits downstream PGC-1α expression by binding to EZH2*

Next, we investigated the downstream target of HIF-1α involved in DR progress. Through mass spectrometry analysis, we identified differentially expressed proteins in RMECs transfected with HIF-1α siRNA or NC under HG conditions (Fig. 4a). Previous studies have indicated that the loss of PGC-1α can cause metabolic dysfunction and retinal degeneration [29,30]. Therefore, we examined the expression of PGC-1α and

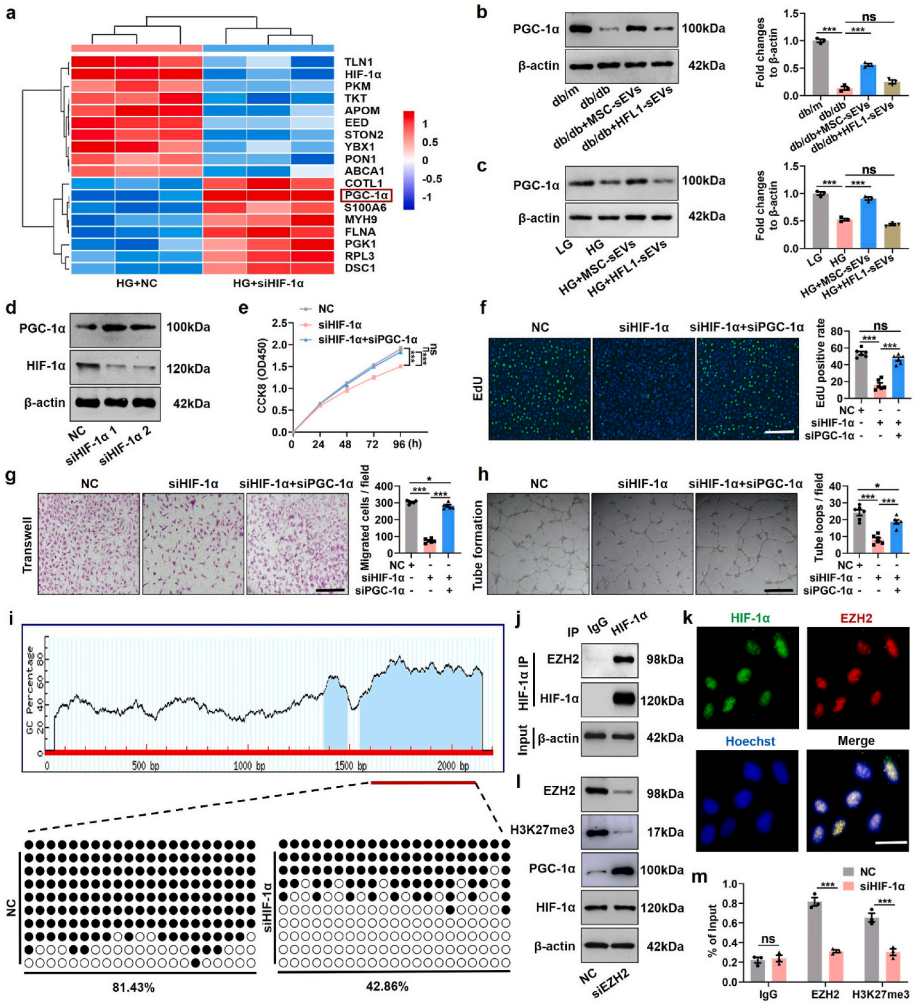

Fig. 4. HIF-1α inhibition promotes PGC-1α expression by reducing EZH2-mediated methylation modification. (**a**) Differentially expressed proteins in RMECs transfected with NC or HIF-1α siRNA. (**b**) Western blot for the retinal expression of PGC-1α. (**c**) Western blot for the expression of PGC-1α in RMECs. (**d**) Western blot for the expression of PGC-1α in RMECs transfected with HIF-1α siRNA. (**e**) CCK8 assay for the proliferation of RMECs (n = 4). (**f**) EdU staining of RMECs (n = 6). Scale bar, 100 μm. (**g**) Transwell assay for the migration of RMECs (n = 6). Scale bar, 100 μm. (**h**) Tube formation assay of RMECs (n = 6). Scale bar, 100 μm. (**i**) BSP analysis of the PGC-1α promoter in NC and HIF-1α siRNA-transfected RMECs. (**j**) Co-IP assay for the binding between HIF-1α and EZH2. (**k**) Immunofluorescence staining images of RMECs showing PGC-1α and EZH2 expressions. Scale bars, 25 μm. (**l**) Western blot for the expressions of HIF-1α, PGC-1α, EZH2 and H3K27me3 in RMECs transfected with EZH2 siRNA. (**m**) ChIP assay for the EZH2 and H3K27me3 binding to the PGC-1α promoter in RMECs transfected with HIF-1α siRNA (n = 3). All data are presented as means ± SEM. ns, not significant, $^{*}P < 0.05$ and $^{***}P < 0.001$.

explored its role in DR. The results of Western blot demonstrated that MSC-sEVs reversed the hyperglycemia-induced downregulation of PGC-1α in retinal tissues (Fig. 4b). Similarly, HG stimulation reduced the PGC-1α level in RMECs, whereas MSC-sEVs promoted the expression of PGC-1α (Fig. 4c). Moreover, HIF-1α knockdown resulted in a significant upregulation of PGC-1α (Fig. 4d), indicating that PGC-1α is negatively regulated by HIF-1α. To determine whether PGC-1α is the downstream target through which HIF-1α contributes to retinal damage, RMECs were co-transfected with HIF-1α siRNA and PGC-1α siRNA. We found that PGC-1α knockdown significantly impaired the functional recovery of RMECs induced by HIF-1α siRNA transfection, characterized by the decreased proliferation, migration, and tube formation (Fig. 4e–h and Supplementary Fig. S5), thereby confirming the essential role of HIF-1α/PGC-1α pathway in DR.

Subsequently, we investigated the interaction mechanism between HIF-1α and PGC-1α. Typical CpG islands were identified to locate in the PGC-1α promoter using the MethPrimer online software, implying that DNA methylation may play a role in the transcriptional regulation of PGC-1α. Subsequently, we conducted BSP assay to detect the methylation status of CpG islands in the promoter region of PGC-1α gene. The results revealed that the CpG islands in the PGC-1α promoter were heavily methylated in RMECs cultured in HG medium, while HIF-1α knockdown substantially reduced the methylation level (Fig. 4i). Because EZH2 is known to be associated with DNA methylation, we investigated whether EZH2 mediated the interaction between HIF-1α and PGC-1α. Co-IP analysis confirmed the binding between HIF-1α and EZH2 (Fig. 4j). The immunofluorescence staining images further demonstrated that HIF-1α was co-localized with EZH2 in the nuclei of RMECs (Fig. 4k). In addition, we transfected EZH2 siRNA into HG medium-cultured RMECs to assess the effect of EZH2 on PGC-1α expression. Western blot analysis revealed that EZH2 knockdown reduced H3K27me3 level and enhanced PGC-1α expression (Fig. 4l). The results of ChIP assay indicated that HIF-1α knockdown suppressed the binding of EZH2 to the promoter of PGC-1α gene and EZH2-mediated H3K27me3 modification (Fig. 4m). Furthermore, overexpression of EZH2 counteracted the recovery of cell function induced by HIF-1α knockdown. Conversely, knockdown of EZH2 further attenuated the proliferation, migration, and tube formation abilities of RMECs which were transfected with HIF-1α siRNA (Supplementary Figs. S6a–f). Collectively, these findings indicate that HIF-1α inhibits downstream

PGC-1α expression through EZH2-mediated epigenetic silencing.

3.5. MSC-sEVs-induced HIF-1α inhibition promotes tripartite motif 21 (TRIM21)-mediated EZH2 ubiquitination and degradation

To further investigate the mechanism underlying the interaction between HIF-1α and EZH2, we examined the effect of HIF-1α on EZH2 expression. The results of Western blot and qRT-PCR showed that HIF-1α siRNA transfection and DMOG treatment significantly altered the expression of EZH2 protein, while EZH2 mRNA levels remained unaffected (Fig. 5a–c), suggesting that HIF-1α may regulate the stability of EZH2 protein. To substantiate this assumption, RMECs were treated with the proteasome inhibitor MG132 and the protein synthesis inhibitor cycloheximide (CHX). We observed that pre-treatment with MG132 prevented the degradation of EZH2 protein induced by HIF-1α knockdown in RMECs (Fig. 5d). Moreover, CHX assay results also demonstrated that HIF-1α knockdown led to a shortened half-life of EZH2 protein (Fig. 5e), indicating the involvement of ubiquitin-proteasome pathway in HIF-1α-mediated regulation of EZH2 protein. Furthermore, Co-IP analysis showed that HIF-1α knockdown enhanced the level of ubiquitinated EZH2 protein, whereas DMOG treatment reduced the ubiquitination modification of EZH2 (Fig. 5f). Subsequently, we performed a Co-IP assay to obtain EZH2-binding proteins and conducted mass spectrometry analysis to determine the protein involved in EZH2 ubiquitination. The results revealed the presence of E3 ubiquitin ligase TRIM21 in EZH2 immunoprecipitation (Fig. 5g). Western blot analysis demonstrated that HIF-1α knockdown or activation did not substantially affect the expression of TRIM21 (Fig. 5h). However, the Co-IP assay showed that HIF-1α inhibition enhanced the interaction between TRIM21 and EZH2, while increased HIF-1α expression reduced the binding of EZH2 to TRIM21 (Fig. 5i). To further verify the role of TRIM21 in the HIF-1α-mediated regulation of EZH2, we blocked TRIM21 in RMECs transfected with HIF-1α siRNA. Co-IP and Western blot results revealed that HIF-1α knockdown-induced EZH2 ubiquitination and degradation could be rescued by TRIM21 inhibition (Fig. 5j and k). Taken together, these findings suggest that HIF-1α inhibition promotes TRIM21-mediated EZH2 ubiquitination and degradation, leading to decreased H3K27me3 modification in the PGC-1α gene.

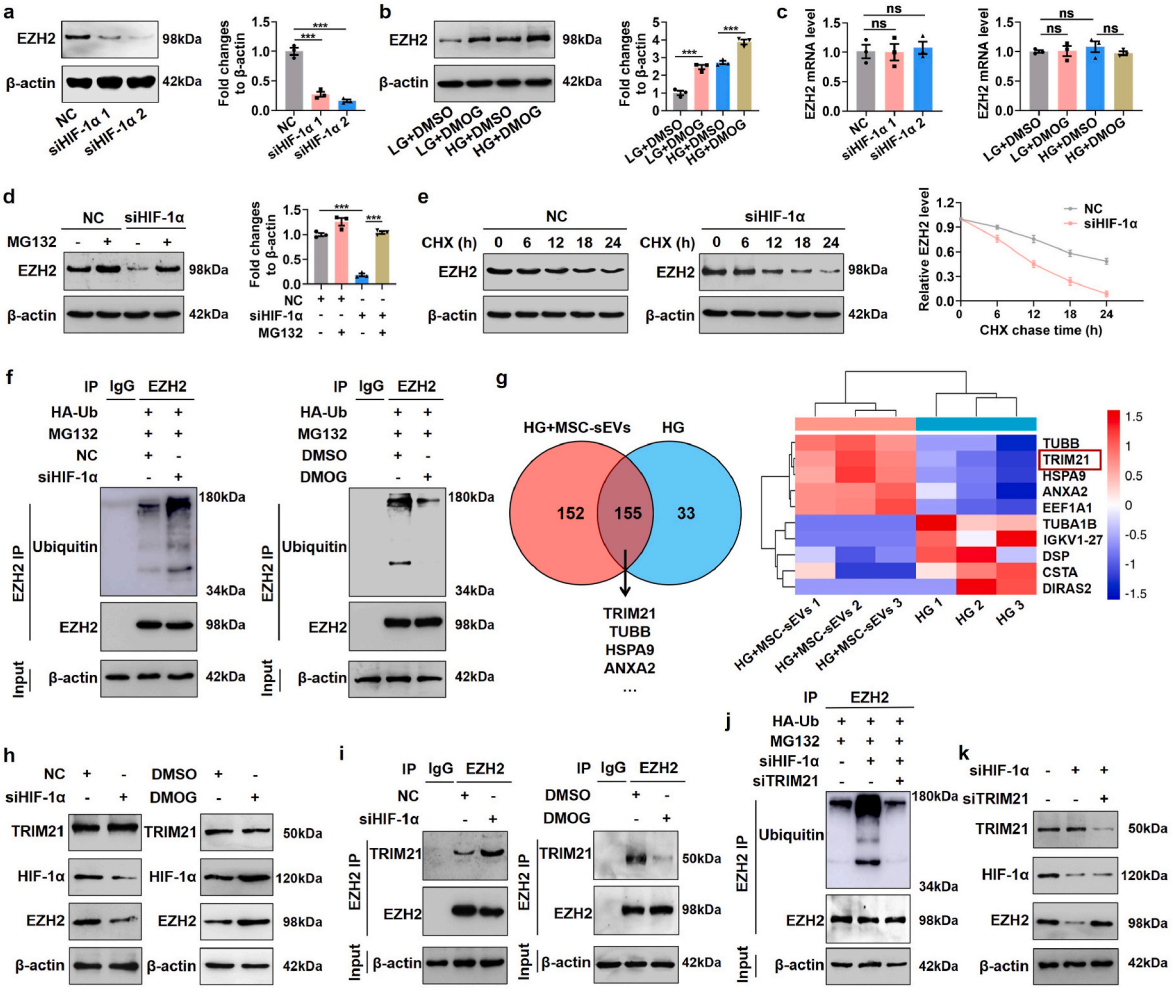

Fig. 5. HIF-1α inhibits TRIM21-mediated EZH2 ubiquitination and degradation. (**a**) Western blot for the expression of EZH2 in RMECs transfected with HIF-1α siRNA. (**b**) Western blot for the expression of EZH2 in RMECs treated with DMOG. (**c**) qRT-PCR for the mRNA level of EZH2 in RMECs treated with HIF-1α siRNA or DMOG. (**d**) Western blot for the effect of MG132 on EZH2 expression in NC and HIF-1α siRNA-transfected RMECs. (**e**) EZH2 expression in NC and HIF-1α siRNA-transfected RMECs was detected at the indicated time points after CHX treatment. (**f**) Co-IP assay for the ubiquitination level of EZH2 in RMECs treated with HIF-1α siRNA or DMOG. (**g**) LC-MS/MS proteomic analysis for the potential interacting proteins of EZH2. (**h**) Western blot for the expression of TRIM21 in RMECs treated with HIF-1α siRNA or DMOG. (**i**) Co-IP assay for the binding of EZH2 to TRIM21 in RMECs treated with HIF-1α siRNA or DMOG. (**j**) Co-IP assay for the ubiquitination level of EZH2 in RMECs transfected with HIF-1α siRNA and TRIM21 siRNA. (**k**) Western blot for the expression of EZH2 in RMECs transfected with HIF-1α siRNA and TRIM21 siRNA. All data are presented as means ± SEM. ns, not significant, $^{***}P < 0.001$.

3.6. MSC-sEVs transport miR-5068 and miR-10228 to target HIF-1α/EZH2/PGC-1α pathway

The long-term effects of MSC-sEVs on retinal tissues suggest the involvement of epigenetic therapeutic mechanisms. It is widely recognized that MSC-sEVs transport miRNAs to regulate the function of recipient cells. To determine the potential miRNAs responsible for the therapeutic roles of MSC-sEVs in this study, we performed miRNA sequencing analysis on MSC-sEVs and HFL1-sEVs and focused on the miRNAs predicted to target HIF-1α (Fig. 6a). Two newly identified miRNAs, miR-5068 and miR-10228, were found to be highly expressed in MSC-sEVs and predicted to interact with HIF-1α mRNA. The results of qRT-PCR confirmed that MSC-sEVs contained significantly higher levels of miR-5068 and miR-10228 compared to HFL1-sEVs (Fig. 6b). We then evaluated the binding interaction between miRNAs and 3′ untranslated regions of HIF-1α mRNA. Dual-luciferase reporter gene analysis showed that transfection with mimics of miR-5068 or miR-10228 reduced the luciferase activity of the wild-type HIF-1α construct but had no effect on the mutant HIF-1α construct, indicating that HIF-1α was a target of miR-5068 and miR-10228 (Fig. 6c and d). Western blot results demonstrated that miR-5068 or miR-10228 mimics transfection suppressed the expressions of HIF-1α and EZH2 and elevated PGC-1α expression in HG medium-cultured RMECs (Fig. 6e). Furthermore, miR-5068 or miR-10228 mimics significantly alleviated the HG-induced enhanced proliferation, migration, and tube formation of RMECs (Fig. 6f–i and Supplementary Fig. S7). Conversely, transfection of miR-5068 or miR-10228 inhibitors had limited effects on the regulation of HIF-1α/EZH2/PGC-1α pathway and cell functions, potentially due to the low content of miR-5068 and miR-10228 in RMECs (Supplementary Figs. S8a–f). These findings indicate that miR-5068 and miR-10228 present in MSC-sEVs possess the ability to alleviate DR by targeting the HIF-1α/EZH2/PGC-1α pathway.

3.7. MiR-5068 and miR-10228 co-mediate the retinal therapeutic effects of MSC-sEVs in db/db mice

To evaluate the role of miR-5068 and miR-10228 in MSC-sEVs-mediated retinal therapy, we loaded inhibitors of miR-5068 and miR-10228 into MSC-sEVs using electroporation to inhibit their activities. Subsequently, db/db mice were intravitreally administered with either natural MSC-sEVs or miRNA inhibitors-loaded MSC-sEVs. The identification results revealed that MSC-sEVs loaded with miRNA inhibitors (MSC-sEVs$^{miRNA\text{-}in}$) retained their characteristic spherical vesicle shape with a slightly increased average diameter and expressed the protein

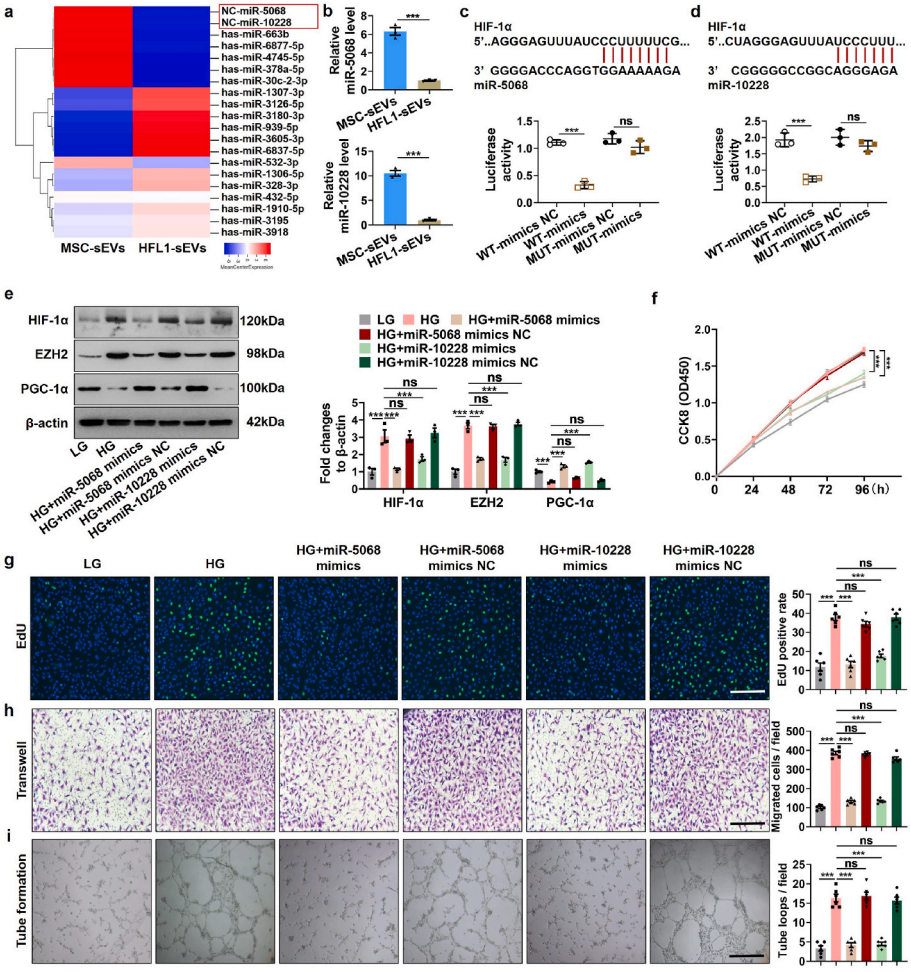

Fig. 6. MSC-sEVs-delivered miR-5068 and miR-10228 target HIF-1α/EZH2/PGC-1α pathway. (**a**) MiRNA sequencing for differentially expressed miRNAs in MSC-sEVs and HFL1-sEVs. (**b**) QRT-PCR for the relative levels of miR-5068 and miR-10228 in MSC-sEVs and HFL1-sEVs (n = 3). Cel-miR-39 was used as the exogenous control. (**c**) Dual-luciferase reporter gene analysis of the binding between HIF-1α and miR-5068 (n = 3). (**d**) Dual-luciferase reporter gene analysis of the binding between HIF-1α and miR-10228 (n = 3). (**e**) Western blot for the expressions of HIF-1α, EZH2 and PGC-1α in RMECs after transfection. (**f**) CCK8 assay for the proliferation of RMECs after transfection (n = 4). (**g**) EdU staining of RMECs after transfection (n = 6). Scale bar, 100 μm. (**h**) Transwell assay for the migration of RMECs after transfection (n = 6). Scale bar, 100 μm. (**i**) Tube formation assay of RMECs after transfection (n = 6). Scale bar, 100 μm. All data are presented as means ± SEM. ns, not significant, ***$P < 0.001$.

markers associated with sEVs (Supplementary Figs. S9a–c). The loading efficiency of MSC-sEVs$^{miR-5068-in}$ group, MSC-sEVs$^{miR-10228-in}$ group and MSC-sEVs$^{miR-5068,10,228-in}$ group was determined to be 71.07 %, 76.27 % and 74.61 % respectively (Supplementary Fig. S9d). Western blot analysis demonstrated that MSC-sEVs$^{miR-5068,10,228-in}$ could not inhibit HIF-1α and EZH2 expressions and elevate PGC-1α level in retinal tissues of db/db mice (Supplementary Fig. S10). Immunofluorescence staining showed that MSC-sEVs$^{miR-5068,10,228-in}$ were able to be absorbed by retinal cells including retinal vascular endothelial cells (Fig. 7a). ERG and OKR analysis demonstrated that the inhibition of miR-5068 or miR-10228 impaired the restorative effects of MSC-sEVs on retinal function (Fig. 7b and Supplementary Fig. S11). H&E staining images showed that the loading of miR-5068 and miR-10228 inhibitors suppressed the therapeutic effects of MSC-sEVs on hyperglycemia-induced retinal degeneration and decreased retinal thickness (Fig. 7c). TUNEL staining and Western blot analysis further demonstrated that miR-5068 and miR-10228 inhibitors weakened the anti-apoptotic potential of MSC-sEVs (Fig. 7d and e). Retinal DHE staining and MDA detection assays provided evidence that the suppression of miR-5068 and miR-10228 diminished the antioxidative properties of MSC-sEVs (Supplementary Figs. S12a–c). Moreover, the administration of miR-5068 and miR-10228 inhibitors resulted in an increased secretion of inflammatory

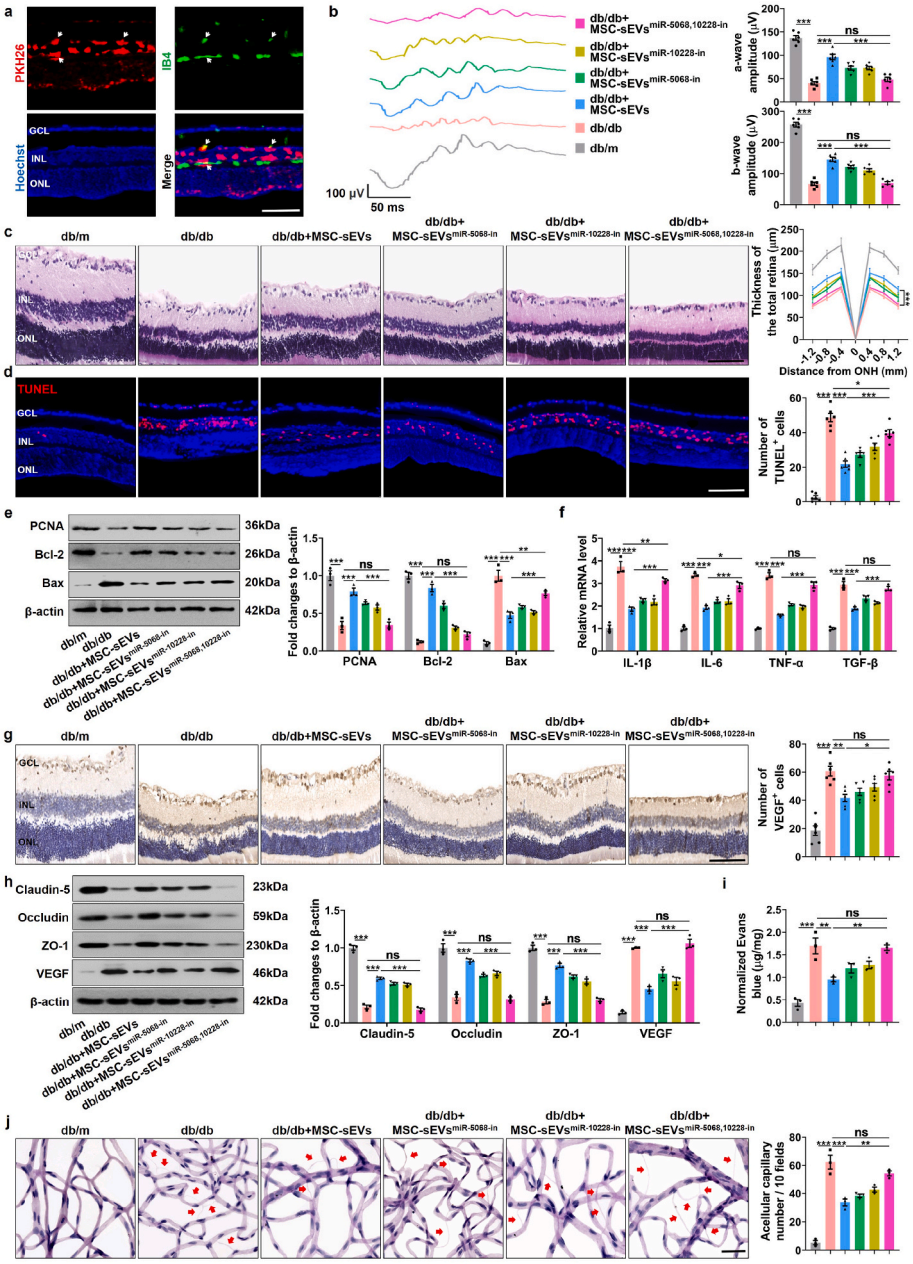

Fig. 7. MiR-5068 and miR-10228 co-mediate retinal therapeutic effects of MSC-sEVs in db/db mice. (**a**) Representative images of retinal sections of db/db mice treated with the PKH26-labeled MSC-sEVs loaded with inhibitors. PKH26, red; IB4, green. Scale bars, 100 μm. (**b**) Representative ERG waveforms and the corresponding analysis of amplitudes of a-wave and b-wave (n = 6). (**c**) H&E staining of retinal tissues and the corresponding quantitative analysis of retinal thickness. Scale bars, 100 μm. (**d**) TUNEL staining of retinal tissues. Scale bars, 100 μm. (**e**) Western blot for the retinal expressions of PCNA, Bcl-2 and Bax. (**f**) qRT-PCR for the relative mRNA levels of IL-1β, IL-6, TNF-α and TGF-β (n = 3). (**g**) Immunohistochemistry images of VEGF in retinal tissues. Scale bars, 100 μm. (**h**) Western blot for the retinal expressions of claudin-5, occludin, ZO-1 and VEGF. (**i**) Quantitative analysis of the residual Evans blue dye in the retina (n = 3). (**j**) Retinal trypsin digestion assay. Scale bar, 50 μm. All data are presented as means ± SEM. ns, not significant, $^{*}P < 0.05$, $^{**}P < 0.01$ and $^{***}P < 0.001$. GCL, ganglion cell layer; INL, inner nuclear layer; ONL, outer nuclear layer.

cytokines compared to MSC-sEVs group (Fig. 7f). Furthermore, MSC-sEVs$^{miR-5068,10,228-in}$ exerted limited effects on reducing VEGF expression, upregulating tight junction proteins, preventing retinal vascular leakage, and alleviating acellular capillary formation (Fig. 7g–j). These findings suggest that miR-5068 and miR-10228 play pivotal roles in the ability of MSC-sEVs to alleviate hyperglycemia-provoked retinal injury.

3.8. Elevated retinal therapeutic efficiency of engineered MSC-sEVs in db/db mice

Considering that the therapeutic effects of MSC-sEVs are mainly associated with the delivery of miR-5068 and miR-10228, we loaded miR-5068 and miR-10228 mimics into MSC-sEVs through electroporation. The results of identification analysis revealed that engineered MSC-sEVs maintained their characteristic cup-shaped morphology with a slight increase in size and expressed the protein markers (Supplementary Figs. S13a–c). The loading efficiency of MSC-sEVs$^{miR-5068}$ group, MSC-sEVs$^{miR-10228}$ group and MSC-sEVs$^{miR-5068,10,228}$ group was determined to be 73.41 %, 69.71 % and 76.67 % respectively (Supplementary Fig. S13d). QRT-PCR analysis confirmed that the levels of miR-5068 and miR-10228 were higher in engineered MSC-sEVs compared to natural MSC-sEVs (Supplementary Fig. S13e), indicating the successful

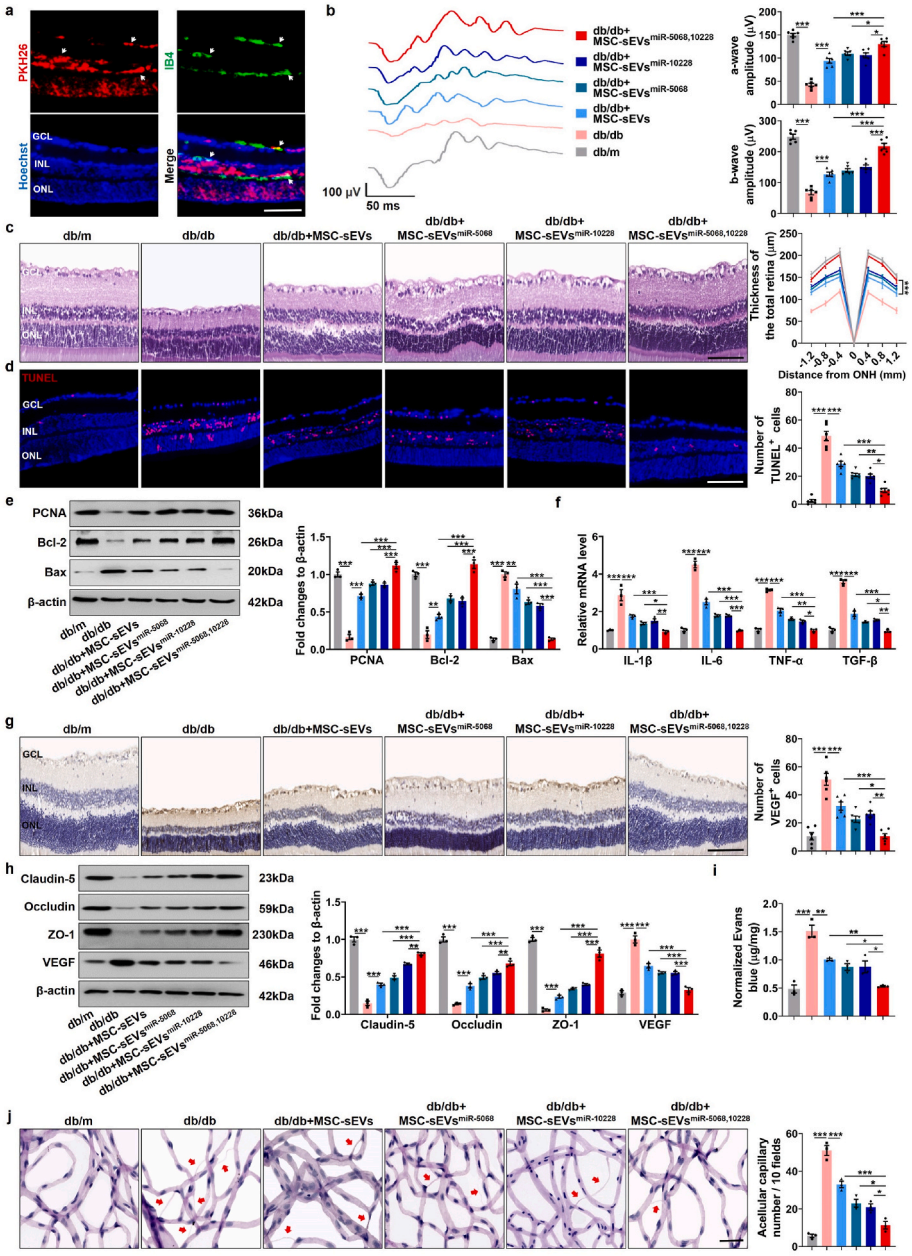

Fig. 8. Elevated retinal therapeutic efficiency of miR-5068 and miR-10228-engineered MSC-sEVs in db/db mice. (**a**) Representative images of retinal sections of db/db mice treated with the PKH26-labeled engineered MSC-sEVs. PKH26, red; IB4, green. Scale bars, 100 μm. (**b**) Representative ERG waveforms and the corresponding analysis of amplitudes of a-wave and b-wave (n = 6). (**c**) H&E staining of retinal tissues and the corresponding quantitative analysis of retinal thickness. Scale bars, 100 μm. (**d**) TUNEL staining of retinal tissues. Scale bars, 100 μm. (**e**) Western blot for the retinal expressions of PCNA, Bcl-2 and Bax. (**f**) qRT-PCR for the relative mRNA levels of IL-1β, IL-6, TNF-α and TGF-β (n = 3). (**g**) Immunohistochemistry images of VEGF in retinal tissues. Scale bars, 100 μm. (**h**) Western blot for the retinal expressions of claudin-5, occludin, ZO-1 and VEGF. (**i**) Quantitative analysis of the residual Evans blue dye in the retina (n = 3). (**j**) Retinal trypsin digestion assay. Scale bar, 50 μm. All data are presented as means ± SEM. ns, not significant, $^{*}P < 0.05$, $^{**}P < 0.01$ and $^{***}P < 0.001$. GCL, ganglion cell layer; INL, inner nuclear layer; ONL, outer nuclear layer.

incorporation of these miRNAs. Furthermore, engineered MSC-sEVs exhibited good stability (Supplementary Fig. S13f). Additionally, an endocytosis experiment demonstrated that engineered MSC-sEVs carrying miRNA mimics could be internalized by RMECs in vitro (Supplementary Fig. S14). Subsequently, we investigated whether engineered MSC-sEVs exhibited enhanced retinal repairing potential in vivo. Western blot analysis demonstrated that the introduction of miR-5068 and miR-10228 mimics enhanced the capability of MSC-sEVs to downregulate the expressions of HIF-1α and EZH2 and upregulate the expression of PGC-1α in retinal tissues (Supplementary Fig. S15). Immunofluorescence staining images provided confirmation of the uptake of engineered MSC-sEVs by retinal cells including retinal vascular endothelial cells (Fig. 8a). In comparison to the MSC-sEVs group, db/db mice treated with miR-5068 and miR-10228-engineered MSC-sEVs exhibited improved electrophysiological function and visual acuity (Fig. 8b and Supplementary Fig. S16). The intravitreal delivery of engineered MSC-sEVs further counteracted diabetic conditions-induced retinal structure disorders and improved retinal thickness (Fig. 8c). Moreover, the elevated levels of miR-5068 and miR-10228 in MSC-sEVs endowed them with enhanced therapeutic effects to mitigate retinal apoptosis, oxidative stress, and inflammation (Fig. 8d–f and Supplementary Figs. S17a–c). Furthermore, MSC-sEVs-mediated vascular protection effect was further strengthened after the loading of miR-5068 and miR-10228, including inhibition of VEGF, upregulation of tight

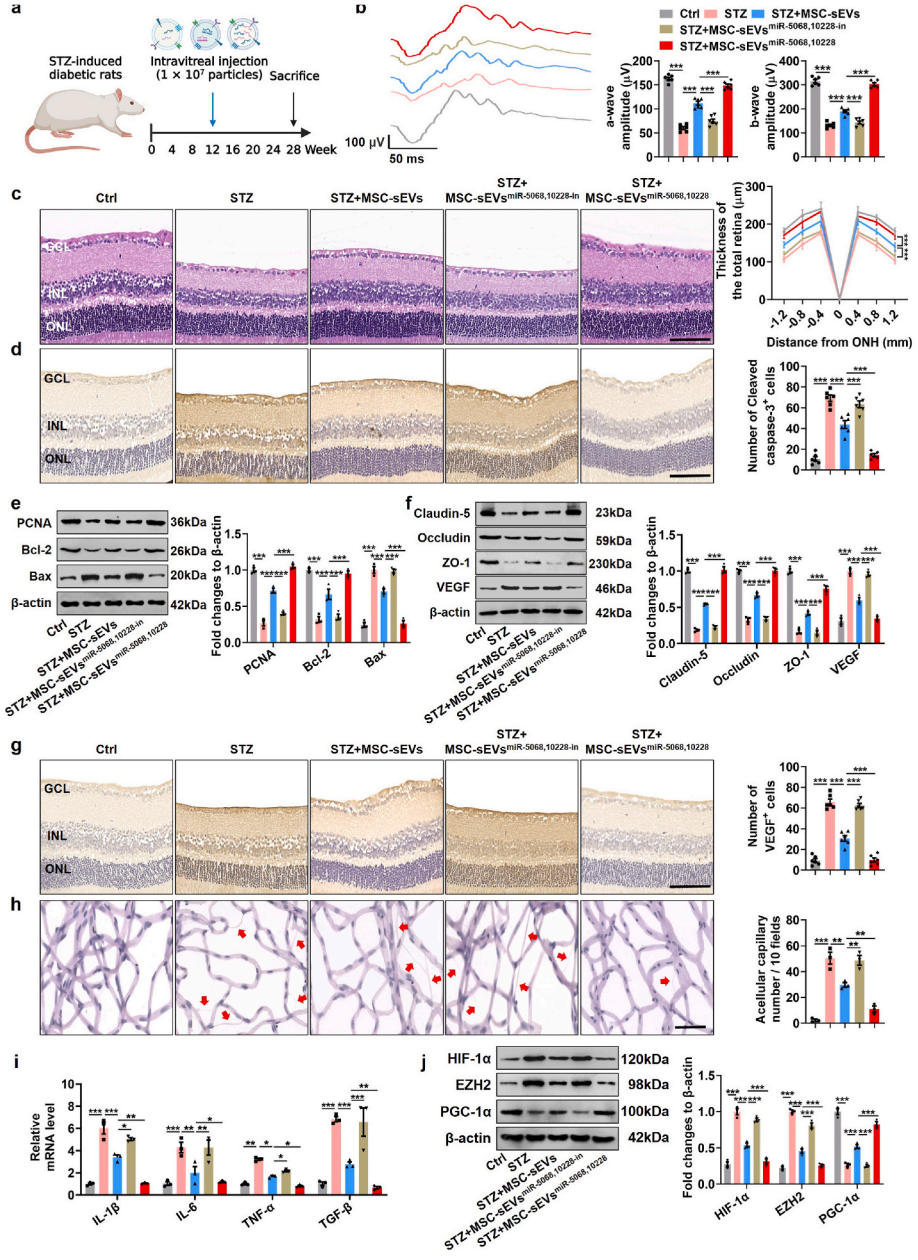

Fig. 9. Retinal therapeutic effects of engineered MSC-sEVs in STZ-induced diabetic rats. (**a**) A schematic diagram showing sEVs administration in STZ-induced diabetic rats. (**b**) Representative ERG waveforms and the corresponding analysis of amplitudes of a-wave and b-wave (n = 6). (**c**) H&E staining of retinal tissues and the corresponding quantitative analysis of retinal thickness. Scale bars, 100 μm. (**d**) Immunohistochemistry images of cleaved caspase-3 in retinal tissues. Scale bars, 100 μm. (**e**) Western blot for the retinal expression of PCNA, Bcl-2 and Bax. (**f**) Western blot for the retinal expression of claudin-5, occludin, ZO-1 and VEGF. (**g**) Immunohistochemistry images of VEGF in retinal tissues. Scale bars, 100 μm. (**h**) Retinal trypsin digestion assay. Scale bar, 50 μm. (**i**) qRT-PCR for the relative mRNA levels of IL-1β, IL-6, TNF-α and TGF-β (n = 3). (**j**) Western blot for the retinal expression of HIF-1α, EZH2 and PGC-1α. All data are presented as means ± SEM. $^{*}P < 0.05$, $^{**}P < 0.01$ and $^{***}P < 0.001$. GCL, ganglion cell layer; INL, inner nuclear layer; ONL, outer nuclear layer.

junction proteins, remission of vascular leakage, and amelioration of neovascularization (Fig. 8g–j). Notably, MSC-sEVs loaded with the mimics of both miR-5068 and miR-10228 exerted stronger effects in retinal therapy compared to the MSC-sEVs loaded with either miR-5068 or miR-10228 mimics, suggesting a synergistic effect between miR-5068 and miR-10228 in promoting retinal protection. Taken together, these findings indicate that miR-5068 and miR-10228-engineered MSC-sEVs exhibit increased therapeutic efficiency for DR compared to natural MSC-sEVs.

3.9. Enhanced retinal therapeutic efficiency of engineered MSC-sEVs in STZ-induced diabetic rats

Next, we injected STZ into high fat diet-fed rats through their tail veins to establish another diabetic animal model. Using this model, we assessed the retinal therapeutic effects of MSC-sEVs, inhibitors-loaded MSC-sEVs and engineered MSC-sEVs (Fig. 9a). In STZ-induced diabetic rats, treatment with MSC-sEVs resulted in improved retinal function, preservation of retinal thickness, and alleviation of retinal apoptosis, oxidative stress, neovascularization, and inflammation (Fig. 9b–i and Supplementary Figs. S18–20). The inhibition of miR-5068 and miR-10228 suppressed the therapeutic effects of MSC-sEVs on hyperglycemia-induced retinal damage. However, the application of engineered MSC-sEVs with higher levels of miR-5068 and miR-10228 enhanced the retinal repair efficiency in STZ-induced diabetic rats, which was attributed to the enhanced regulation of the HIF-1α/EZH2/PGC-1α pathway (Fig. 9j). Overall, these findings demonstrate the effective therapeutic effects of engineered MSC-sEVs in treating retinal damage in two diabetic animal models, db/db mice and STZ-induced diabetic rats.

4. Discussion

Retinal endothelial cell dysfunction plays a crucial role in the development of DR. However, treatment options are limited [31,32]. The secretion of sEVs has been identified as the primary mechanism of MSC to exert therapeutic effects [33]. Importantly, the cell-free superiority of MSC-sEVs makes them promising candidates for retinal protection. In this study, we assessed the feasibility and effectiveness of MSC-sEVs for DR therapy. We injected MSC-sEVs into db/db mice and STZ-induced diabetic rats through intravitreal administration. Db/db mice have a mutation in the leptin receptor, while STZ disrupts pancreatic islets and causes β cell loss. Both animal models are commonly used to study DR [34]. Although the mechanisms for inducing diabetes are different between these models, the long-term exposure to hyperglycemia leads to retinal damage in both cases. Previous studies have shown that both db/db mice and STZ-induced diabetic animals exhibit similar characteristics of retinal damage after 6 months [35–37]. Therefore, we selected these animal models to investigate whether MSC-sEVs can provide therapeutic benefits for retinal damage caused by different mechanisms-induced hyperglycemia. Our results demonstrated that MSC-sEVs exerted similar effects to improve retinal function and reduce hyperglycemia-induced retinal apoptosis, inflammation, and angiogenesis in both animal models, suggesting that MSC-sEVs have the potential to mitigate retinal injury caused by hyperglycemia resulting from various pathological processes.

Transfer of miRNAs through MSC-sEVs has been widely recognized as a significant contributor to tissue regeneration [38]. In the ocular system, miRNAs present in MSC-sEVs can be efficiently absorbed by recipient cells, where they can consistently regulate cellular pathophysiological processes [39]. MiRNA-dependent mechanism is also essential for the therapeutic potential of MSC-sEVs in treating retinitis pigmentosa and optic nerve injury [40,41]. In this study, two novel miRNAs, miR-5068 and miR-10228, were found to be abundant in MSC-sEVs and responsible for the inhibition of HIF-1α. The functional inhibition of miR-5068 and miR-10228 nullified the retinal therapeutic effects of MSC-sEVs, thus confirming that MSC-sEVs alleviate DR mainly through the delivery of miR-5068 and miR-10228.

sEVs serve as a natural delivery platform for transporting drugs and therapeutic molecules [42]. Recent studies have focused on the development of engineering strategies for sEVs to enhance their therapeutic efficiency and targeting capability. Engineered sEVs prepared using various techniques such as exogenous cargo loading and membrane decoration have shown elevated therapeutic potential in treating retinal disorders [43,44]. These advancements in engineering sEVs offer promising avenues for improving the efficacy of therapeutic interventions in retinal diseases. For instance, Tian et al. have reported that regulatory T cells-derived sEVs conjugated with the anti-VEGF antibody accumulate in the neovascularization lesions and markedly suppress ocular neovascularization [45]. The findings of Reddy et al. have demonstrated that sEVs-loaded with anti-VEGF drug bevacizumab can significantly reduce the frequency of intravitreal injection required for the treatment of DR [46]. Mathew et al. have also revealed that engineering miR-424 into sEVs can enhance their therapeutic potential in treating retinal ischemic disorders [24]. Based on these findings, we incorporated miR-5068 and miR-10228 into MSC-sEVs to augment the levels of therapeutic miRNAs. Remarkably, compared to natural MSC-sEVs, MSC-sEVs engineered with miR-5068 and miR-10228 demonstrated heightened therapeutic capabilities in mitigating retinal injury both in db/db mice and STZ-induced diabetic rats.

As a crucial regulatory gene under hypoxic conditions, HIF-1α plays a significant role in coordinating various cellular processes [47]. Previous studies have demonstrated that the level of HIF-1α is notably elevated in the vitreous fluid of patients with proliferative DR [48]. The activation of HIF-1α is closely associated with pathological retinal angiogenesis [49]. Our study showed that MSC-sEVs effectively inhibited diabetic stimulation-induced HIF-1α upregulation. Treatment with the HIF-1α agonist significantly reduced MSC-sEVs-induced protective effects, suggesting that MSC-sEVs alleviate DR mainly by inhibiting HIF-1α. Thus, our findings support HIF-1α as an important target for DR therapy. However, the exact molecular mechanism through which HIF-1α contributes to retinal injury remains unclear. Accumulating studies have demonstrated that PGC-1α is a crucial regulatory gene in energy metabolism [50]. Upregulation of PGC-1α can attenuate ROS production, inflammation, and vascular dysfunction [51,52]. Mice lacking PGC-1α exhibit a loss of pericyte coverage, injured retinal vascular plexuses, and extensive retinal hemorrhaging [53]. Through mass spectrometry analysis, we identified elevated PGC-1α expression in RMECs treated with HIF-1α siRNA. Further studies revealed that the inhibition of PGC-1α substantially impaired the functional recovery of retinal cells induced by HIF-1α knockdown, suggesting that PGC-1α is a downstream target of HIF-1α in the progression of DR.

As a histone methyltransferase, EZH2 is the functional component of the polycomb repressive complex 2 [54]. EZH2 affects DNA methylation in gene promoters through H3K27me3 modification [55]. However, it is still unknown whether EZH2 is involved in tissue regeneration, particularly in the therapy of DR. In this study, we found that HIF-1α inhibited PGC-1α expression through EZH2-mediated methylation of the PGC-1α promoter. Experiments with MG132 and CHX revealed that HIF-1α regulated EZH2 protein stability mainly through the ubiquitin-proteasome pathway. Previous studies have indicated that ubiquitin modification represents a major mechanism for modulating EZH2 expression and activity [56]. Several E3 ligases, such as tumor necrosis factor receptor-associated factor 6, β-transducin repeats-containing protein and SMAD-specific E3 ubiquitin protein ligase 2, have been reported to be involved in the ubiquitination of EZH2 [57–59]. Through mass spectrometry analysis, we discovered that HIF-1α knockdown promoted the interaction between EZH2 and TRIM21, leading to the degradation of EZH2. The knockdown of TRIM21 reversed the increased ubiquitination of EZH2 induced by HIF-1α inhibition.

However, it is important to note that the rodent models used to study

DR have certain limitations in replicating disease progression and accurately representing the human condition. Therefore, alternative options such as nonhuman primate models and studies involving human patients with DR should be considered for determining the dosage, injection timing, and injection method of MSC-sEVs. Further investigations are essential to fully explore and understand the clinical applicability of MSC-sEVs in DR therapy.

5. Conclusions

In summary, our findings demonstrate that MSC-sEVs can alleviate hyperglycemia-induced retinal injury through miR-5068 and miR-10228-mediated inhibition of HIF-1α pathway. Downregulation of HIF-1α promotes TRIM21-mediated EZH2 ubiquitination, resulting in the reduced methylation modification in the PGC-1α gene promoter. Importantly, engineered MSC-sEVs with higher levels of miR-5068 and miR-10228 exhibit enhanced therapeutic potential. Therefore, this study not only elucidates the molecular mechanism underlying the retinal protective effects of MSC-sEVs, but also establishes engineered MSC-sEVs as a promising DR treatment strategy.

Data availability

The datasets used and/or analyzed during the current study are available from the corresponding author on reasonable request.

Ethics approval and consent to participate

The study was approved by the Ethics Committee for Experimental Animals of Jiangsu University (UJS-IACUC-2021110301).

CRediT authorship contribution statement

Fengtian Sun: Conceptualization, Data curation, Formal analysis, Investigation, Methodology, Visualization, Writing – original draft. **Yuntong Sun:** Investigation, Methodology. **Xiaoling Wang:** Investigation, Methodology. **Junyan Zhu:** Investigation. **Shenyuan Chen:** Investigation. **Yifan Yu:** Investigation. **Mengyao Zhu:** Methodology. **Wenrong Xu:** Conceptualization, Funding acquisition, Supervision, Writing – review & editing. **Hui Qian:** Conceptualization, Data curation, Funding acquisition, Supervision, Writing – review & editing.

Declaration of competing interest

All authors declare that they have no conflicts of interest and no competing interest.

Acknowledgements

This work was supported by the National Natural Science Foundation of China (81971757, 82272179), the Advanced Science and Technology Foundation of the Jiangsu Province (BE2021689), Zhenjiang Key Laboratory of High Technology Research on Exosomes Foundation and Transformation Application (ss2018003), and Priority Academic Program Development of Jiangsu Higher Education Institutions Project (Phase III).

Appendix A. Supplementary data

Supplementary data to this article can be found online at https://doi.org/10.1016/j.bioactmat.2023.11.008.

References

[1] C.C. Wykoff, R.N. Khurana, Q.D. Nguyen, S.P. Kelly, F. Lum, R. Hall, I.M. Abbass, A.M. Abolian, I. Stoilov, T.M. To, V. Garmo, Risk of blindness among patients with diabetes and newly diagnosed diabetic retinopathy, Diabetes Care 44 (2021) 748–756.
[2] S.R. Levine, P. Sapieha, S. Dutta, J.K. Sun, T.W. Gardner, It is time for a moonshot to find "Cures" for diabetic retinal disease, Prog. Retin. Eye Res. 90 (2022), 101051.
[3] D.A. Antonetti, P.S. Silva, A.W. Stitt, Current understanding of the molecular and cellular pathology of diabetic retinopathy, Nat. Rev. Endocrinol. 17 (2021) 195–206.
[4] J. Hu, S. Dziumbla, J. Lin, S.I. Bibli, S. Zukunft, J. de Mos, K. Awwad, T. Frömel, A. Jungmann, K. Devraj, Z. Cheng, L. Wang, S. Fauser, C.G. Eberhart, A. Sodhi, B. D. Hammock, S. Liebner, O.J. Müller, C. Glaubitz, H.P. Hammes, R. Popp, I. Fleming, Inhibition of soluble epoxide hydrolase prevents diabetic retinopathy, Nature 552 (2017) 248–252.
[5] Z. Xie, X.J. Wu, R.W. Cheng, J.H. Cui, S.T. Yuan, J.W. Zhou, Q.H. Liu, JP1, a polypeptide specifically targeting integrin αVβ3, ameliorates choroidal neovascularization and diabetic retinopathy in mice, Acta Pharmacol. Sin. 44 (2022) 897–912.
[6] J.H. Wu, Y.N. Li, A.Q. Chen, C.D. Hong, C.L. Zhang, H.L. Wang, Y.F. Zhou, P.C. Li, Y. Wang, L. Mao, Y.P. Xia, Q.W. He, H.J. Jin, Z.Y. Yue, B. Hu, Inhibition of Sema4D/PlexinB1 signaling alleviates vascular dysfunction in diabetic retinopathy, EMBO Mol. Med. 12 (2020), e10154.
[7] K.J. Wert, V.B. Mahajan, L. Zhang, Y. Yan, Y. Li, J. Tosi, C.W. Hsu, T. Nagasaki, K. M. Janisch, M.B. Grant, M. Mahajan, A.G. Bassuk, S.H. Tsang, Neuroretinal hypoxic signaling in a new preclinical murine model for proliferative diabetic retinopathy, Signal Transduct. Targeted Ther. 1 (2016), 16005.
[8] G.S. Tan, U. Chakravarthy, T.Y. Wong, Anti-VEGF therapy or vitrectomy surgery for vitreous hemorrhage from proliferative diabetic retinopathy, JAMA 324 (2020) 2375–2377.
[9] Q. Jiang, C. Liu, C.P. Li, S.S. Xu, M.D. Yao, H.M. Ge, Y.N. Sun, X.M. Li, S.J. Zhang, K. Shan, B.H. Liu, J. Yao, C. Zhao, B. Yan, Circular RNA-ZNF532 regulates diabetes-induced retinal pericyte degeneration and vascular dysfunction, J. Clin. Invest. 130 (2020) 3833–3847.
[10] G. Mannino, C. Russo, A. Longo, C.D. Anfuso, G. Lupo, D. Lo Furno, R. Giuffrida, G. Giurdanella, Potential therapeutic applications of mesenchymal stem cells for the treatment of eye diseases, World J. Stem Cell. 13 (2021) 632–644.
[11] C.R. Harrell, V. Djonov, V. Volarevic, Therapeutic potential of mesenchymal stem cells in the treatment of ocular graft-versus-host disease, Int. J. Mol. Sci. 23 (2022), 13254.
[12] H.Y. Lee, I.S. Hong, Double-edged sword of mesenchymal stem cells: cancer-promoting versus therapeutic potential, Cancer Sci. 108 (2017) 1939–1946.
[13] A. Aneesh, A. Liu, H.E. Moss, D. Feinstein, S. Ravindran, B. Mathew, S. Roth, Emerging concepts in the treatment of optic neuritis: mesenchymal stem cell-derived extracellular vesicles, Stem Cell Res. Ther. 12 (2021) 594.
[14] G. van Niel, D.R.F. Carter, A. Clayton, D.W. Lambert, G. Raposo, P. Vader, Challenges and directions in studying cell-cell communication by extracellular vesicles, Nat. Rev. Mol. Cell Biol. 23 (2022) 369–382.
[15] J. Janockova, L. Slovinska, D. Harvanova, T. Spakova, J. Rosocha, New therapeutic approaches of mesenchymal stem cells-derived exosomes, J. Biomed. Sci. 28 (2021) 39.
[16] A. Nagelkerke, M. Ojansivu, L. van der Koog, T.E. Whittaker, E.M. Cunnane, A. M. Silva, N. Dekker, M.M. Stevens, Extracellular vesicles for tissue repair and regeneration: evidence, challenges and opportunities, Adv. Drug Deliv. Rev. 175 (2021), 113775.
[17] B. Mathew, S. Ravindran, X. Liu, L. Torres, M. Chennakesavalu, C.C. Huang, L. Feng, R. Zelka, J. Lopez, M. Sharma, S. Roth, Mesenchymal stem cell-derived extracellular vesicles and retinal ischemia-reperfusion, Biomaterials 197 (2019) 146–160.
[18] F. Sun, Y. Sun, J. Zhu, X. Wang, C. Ji, J. Zhang, S. Chen, Y. Yu, W. Xu, H. Qian, Mesenchymal stem cells-derived small extracellular vesicles alleviate diabetic retinopathy by delivering NEDD4, Stem Cell Res. Ther. 13 (2022) 293.
[19] I.K. Herrmann, M.J.A. Wood, G. Fuhrmann, Extracellular vesicles as a next-generation drug delivery platform, Nat. Nanotechnol. 16 (2021) 748–759.
[20] X. Zhang, H. Zhang, J. Gu, J. Zhang, H. Shi, H. Qian, D. Wang, W. Xu, J. Pan, H. A. Santos, Engineered extracellular vesicles for cancer therapy, Adv. Mater. 33 (2021), e2005709.
[21] J. Chen, Q. Tan, Z. Yang, Y. Jin, Engineered extracellular vesicles: potentials in cancer combination therapy, J. Nanobiotechnol. 20 (2022) 132.
[22] L. Ohayon, X. Zhang, P. Dutta, The role of extracellular vesicles in regulating local and systemic inflammation in cardiovascular disease, Pharmacol. Res. 170 (2021), 105692.
[23] C.L. Deng, C.B. Hu, S.T. Ling, N. Zhao, L.H. Bao, F. Zhou, Y.C. Xiong, T. Chen, B. D. Sui, X.R. Yu, C.H. Hu, Photoreceptor protection by mesenchymal stem cell transplantation identifies exosomal MiR-21 as a therapeutic for retinal degeneration, Cell Death Differ. 28 (2021) 1041–1061.
[24] B. Mathew, L.G. Acha, L.A. Torres, C.C. Huang, A. Liu, S. Kalinin, K. Leung, Y. Dai, D.L. Feinstein, S. Ravindran, S. Roth, MicroRNA-based engineering of mesenchymal stem cell extracellular vesicles for treatment of retinal ischemic disorders: engineered extracellular vesiclesand retinal ischemia, Acta Biomater. 158 (2023) 782–797.
[25] A. Mazzeo, T. Lopatina, C. Gai, M. Trento, M. Porta, E. Beltramo, Functional analysis of miR-21-3p, miR-30b-5p and miR-150-5p shuttled by extracellular vesicles from diabetic subjects reveals their association with diabetic retinopathy, Exp. Eye Res. 184 (2019) 56–63.
[26] Y. Zeng, X. Yao, X. Liu, X. He, L. Li, X. Liu, Z. Yan, J. Wu, B.M. Fu, Anti-angiogenesis triggers exosomes release from endothelial cells to promote tumor vasculogenesis, J. Extracell. Vesicles 8 (2019), 1629865.

[27] S. Mudaliar, C. Hupfeld, D.L. Chao, SGLT2 Inhibitor-induced low-grade ketonemia ameliorates retinal hypoxia in diabetic retinopathy-a novel hypothesis, J. Clin. Endocrinol. Metab. 106 (2021) 1235–1244.
[28] H.Y. Li, Y. Yuan, Y.H. Fu, Y. Wang, X.Y. Gao, Hypoxia-inducible factor-1α: a promising therapeutic target for vasculopathy in diabetic retinopathy, Pharmacol. Res. 159 (2020), 104924.
[29] D.Y. Shu, E.R. Butcher, M. Saint-Geniez, Suppression of PGC-1α drives metabolic dysfunction in TGFβ2-induced EMT of retinal pigment epithelial cells, Int. J. Mol. Sci. 22 (2021) 4701.
[30] M.A.B. Rosales, D.Y. Shu, J. Iacovelli, M. Saint-Geniez, Loss of PGC-1α in RPE induces mesenchymal transition and promotes retinal degeneration, Life Sci. Alliance 2 (2019), e201800212.
[31] C. Gu, X. She, C. Zhou, T. Su, S. He, C. Meng, Q. Gu, D. Luo, Z. Zheng, Q. Qiu, Dihydroartemisinin ameliorates retinal vascular dysfunction in diabetes mellitus via the FASN/Kmal-mTOR/SREBP1 feedback loop, Pharmacol. Res. 174 (2021), 105871.
[32] G. Yang, J. Wei, P. Liu, Q. Zhang, Y. Tian, G. Hou, L. Meng, Y. Xin, X. Jiang, Role of the gut microbiota in type 2 diabetes and related diseases, Metabolism 117 (2021), 154712.
[33] A. Rahmani, K. Saleki, N. Javanmehr, J. Khodaparast, P. Saadat, H.R. Nouri, Mesenchymal stem cell-derived extracellular vesicle-based therapies protect against coupled degeneration of the central nervous and vascular systems in stroke, Ageing Res. Rev. 62 (2020), 101106.
[34] A.M. Olivares, K. Althoff, G.F. Chen, S. Wu, M.A. Morrisson, M.M. DeAngelis, N. Haider, Animal models of diabetic retinopathy, Curr. Diabetes Rep. 17 (2017) 93.
[35] S.R. Sheskey, D.A. Antonetti, R.C. Rentería, C.M. Lin, Correlation of retinal structure and cisual function assessments in mouse diabetes models, Invest. Ophthalmol. Vis. Sci. 62 (2021) 20.
[36] I.S. Samuels, B.A. Bell, A. Pereira, J. Saxon, N.S. Peachey, Early retinal pigment epithelium dysfunction is concomitant with hyperglycemia in mouse models of type 1 and type 2 diabetes, J. Neurophysiol. 113 (2015) 1085–1099.
[37] T. Azrad-Leibovich, A. Zahavi, M.F. Gohas, M. Brookman, O. Barinfeld, O. Muhsinoglu, S. Michowiz, D. Fixler, N. Goldenberg-Cohen, Characterization of diabetic retinopathy in two mouse models and response to a single injection of anti-vascular endothelial growth factor, Int. J. Mol. Sci. 24 (2022) 324.
[38] M.I. Nasser, M. Masood, S. Adlat, D. Gang, S. Zhu, G. Li, N. Li, J. Chen, P. Zhu, Mesenchymal stem cell-derived exosome microRNA as therapy for cardiac ischemic injury, Biomed. Pharmacother. 143 (2021), 112118.
[39] B. Mead, S. Tomarev, Bone marrow-derived mesenchymal stem cells-derived exosomes promote survival of retinal ganglion cells through miRNA-dependent mechanisms, Stem Cells Transl. Med. 6 (2017) 1273–1285.
[40] J. Zhang, P. Li, G. Zhao, S. He, D. Xu, W. Jiang, Q. Peng, Z. Li, Z. Xie, H. Zhang, Y. Xu, L. Qi, Mesenchymal stem cell-derived extracellular vesicles protect retina in a mouse model of retinitis pigmentosa by anti-inflammation through miR-146a-Nr4a3 axis, Stem Cell Res. Ther. 13 (2022) 394.
[41] X. Sang, L. Tang, L. Zhao, N. Xu, F. Liu, Y. Shen, W. Wei, Y. Cheng, W. Huang, Y. Liu, Y. Su, C. Xu, Y. Li, Z. Wang, S. Liu, Umbilical cord mesenchymal stem cell-derived exosomes promote axon regeneration during optic nerve injury through microRNA-dependent mTORC1 signalling, Clin. Transl. Med. 13 (2023) e1319.
[42] G. Zhang, X. Huang, H. Xiu, Y. Sun, J. Chen, G. Cheng, Z. Song, Y. Peng, Y. Shen, J. Wang, Z. Cai, Extracellular vesicles: natural liver-accumulating drug delivery vehicles for the treatment of liver diseases, J. Extracell. Vesicles 10 (2020), e12030.
[43] M.K. Jayasinghe, M. Tan, B. Peng, Y. Yang, G. Sethi, M. Pirisinu, M.T.N. Le, New approaches in extracellular vesicle engineering for improving the efficacy of anti-cancer therapies, Semin. Cancer Biol. 74 (2021) 62–78.
[44] L. Nieland, S. Mahjoum, E. Grandell, K. Breyne, X.O. Breakefield, Engineered EVs designed to target diseases of the CNS, J. Contr. Release 356 (2023) 493–506.
[45] Y. Tian, F. Zhang, Y. Qiu, S. Wang, F. Li, J. Zhao, C. Pan, Y. Tao, D. Yu, W. Wei, Reduction of choroidal neovascularization via cleavable VEGF antibodies conjugated to exosomes derived from regulatory T cells, Nat. Biomed. Eng. 5 (2021) 968–982.
[46] S.K. Reddy, A.R. Ballal, S. Shailaja, R.N. Seetharam, C.H. Raghu, R. Sankhe, K. Pai, T. Tender, M. Mathew, A. Aroor, A.K. Shetty, S. Adiga, V. Devi, M.S. Muttigi, D. Upadhya, Small extracellular vesicle-loaded bevacizumab reduces the frequency of intravitreal injection required for diabetic retinopathy, Theranostics 13 (2023) 2241–2255.
[47] S.B. Catrina, X. Zheng, Hypoxia and hypoxia-inducible factors in diabetes and its complications, Diabetologia 64 (2021) 709–716.
[48] S. Loukovaara, P. Koivunen, M. Inglés, J. Escobar, M. Vento, S. Andersson, Elevated protein carbonyl and HIF-1α levels in eyes with proliferative diabetic retinopathy, Acta Ophthalmol. 92 (2014) 323–327.
[49] Y.H. Huang, C.H. Kuo, I.C. Peng, Y.S. Chang, S.H. Tseng, E.M. Conway, H.L. Wu, Recombinant thrombomodulin domain 1 rescues pathological angiogenesis by inhibition of HIF-1α-VEGF pathway, Cell. Mol. Life Sci. 78 (2021) 7681–7692.
[50] N. Naumenko, M. Mutikainen, L. Holappa, J.L. Ruas, T. Tuomainen, P. Tavi, PGC-1α deficiency reveals sex-specific links between cardiac energy metabolism and EC-coupling during development of heart failure in mice, Cardiovasc. Res. 118 (2021) 1520–1534.
[51] X. Gan, J. Zhao, Y. Chen, Y. Li, B. Xuan, M. Gu, F. Feng, Y. Yang, D. Yang, X. Sun, Plin5 inhibits proliferation and migration of vascular smooth muscle cell through interacting with PGC-1α following vascular injury, Bioengineered 13 (2022) 10665–10678.
[52] X. Fu, J. Jiao, T. Qin, J. Yu, Q. Fu, X. Deng, S. Ma, Z. Ma, A new perspective on ameliorating depression-like behaviors: suppressing neuroinflammation by upregulating PGC-1α, Neurotox. Res. 39 (2021) 872–885.
[53] N. García-Quintans, C. Sánchez-Ramos, I. Prieto, A. Tierrez, E. Arza, A. Alfranca, J. M. Redondo, M. Monsalve, Oxidative stress induces loss of pericyte coverage and vascular instability in PGC-1α-deficient mice, Angiogenesis 19 (2016) 217–228.
[54] S. Choufani, W.T. Gibson, A.L. Turinsky, B.H.Y. Chung, T. Wang, K. Garg, A. Vitriolo, A.S.A. Cohen, S. Cyrus, S. Goodman, E. Chater-Diehl, J. Brzezinski, M. Brudno, L.H. Ming, S.M. White, S.A. Lynch, C. Clericuzio, I.K. Temple, F. Flinter, V. McConnell, T. Cushing, L.M. Bird, M. Splitt, B. Kerr, S.W. Scherer, J. Machado, E. Imagawa, N. Okamoto, N. Matsumoto, G. Testa, M. Iascone, R. Tenconi, O. Caluseriu, R. Mendoza-Londono, D. Chitayat, C. Cytrynbaum, K. Tatton-Brown, R. Weksberg, DNA methylation signature for EZH2 functionally classifies sequence variants in three PRC2 complex genes, Am. J. Hum. Genet. 106 (2020) 596–610.
[55] L. Yang, D.W. Ma, Y.P. Cao, D.Z. Li, X. Zhou, J.F. Feng, J. Bao, PRMT5 functionally associates with EZH2 to promote colorectal cancer progression through epigenetically repressing CDKN2B expression, Theranostics 11 (2021) 3742–3759.
[56] W. Lu, F. Cao, L. Feng, G. Song, Y. Chang, Y. Chu, Z. Chen, B. Shen, H. Xu, S. Wang, J. Ma, LncRNA Snhg6 regulates the differentiation of MDSCs by regulating the ubiquitination of EZH2, J. Hematol. Oncol. 14 (2021) 196.
[57] Z. Li, D. Wang, J. Lu, B. Huang, Y. Wang, M. Dong, D. Fan, H. Li, Y. Gao, P. Hou, M. Li, H. Liu, Z.Q. Pan, J. Zheng, J. Bai, Methylation of EZH2 by PRMT1 regulates its stability and promotes breast cancer metastasis, Cell Death Differ. 27 (2020) 3226–3242.
[58] A.A. Sahasrabuddhe, X. Chen, F. Chung, T. Velusamy, M.S. Lim, K.S. Elenitoba-Johnson, Oncogenic Y641 mutations in EZH2 prevent Jak2/β-TrCP-mediated degradation, Oncogene 34 (2015) 445–454.
[59] K. Liao, S. Deng, L. Xu, W. Pan, S. Yang, F. Zheng, X. Wu, H. Hu, Z. Liu, J. Luo, R. Zhang, D.M. Kuang, J. Dong, Y. Wu, H. Zhang, P. Zhou, J.X. Bei, Y. Xu, Y. Ji, P. Wang, H.Q. Ju, R.H. Xu, B. Li, A feedback circuitry between polycomb signaling and fructose-1, 6-bisphosphatase enables hepatic and renal tumorigenesis, Cancer Res. 80 (2020) 675–688.